Endosymbiotic bioenergetic synergy behind adaptation and speciation of rainforest warblers

Dahong Chen[1]*, Silu Wang[2]*
[1]Department of Biochemistry
Jacobs School of Medicine & Biomedical Sciences
State University of New York, Buffalo

[2] Department of Biological Sciences
State University of New York, Buffalo
*co-corresponding author email: siluwang.biodiv@gmail.com

Abstract

The molecular genetic cooperation among organelles facilitates adaptation during eukaryotic evolution, but the composition of such endosymbiotic synergy in the organismal adaptation and speciation remains unclear. The speciating wood warblers hybridizing in the Pacific Rainforest experiencing dramatic climate changes provide natural inter-organelle-recombination experiments to understand the molecular genomic processes associated with speciation and adaptation in the changing world. Integrating life history morphometrics, cell-type-specific multiomics, biochemical analyses and confocal imaging, we discovered the endosymbiotic bioenergetic synergy among nucleus, mitochondria, and ribosome at the molecular genomic frontier of divergent climate adaptation. We further identified signatures of adaptive inertia in populations underwent drastic climate change, which corresponds with endosymbiotic uncoupling and reduced energy capacity. Remarkably, endosymbiotic co-transcriptional synergy can be rescued by the introgression of warm-adapted endosymbiotic genetic variants across the species boundaries despite the risk of endosymbiotic bioenergetic incompatibility brought by ancestry discordance. This study inspires the Endosymbiotic Bioenergetic Synergy Model, which characterizes the molecular genomic cofunction, co-regulation, coevolution, and co-introgression among organelles underlying bioenergetic adaptation and speciation of eukaryotes. This endosymbiotic synergistic insight illuminates further investigation of bioenergetic adaptation of eukaryotic species over space and time.

Introduction

Cytonuclear coevolution facilitates organismal adaptation on our changing planet since the endosymbiotic origin of eukaryotes over 2 billion years ago[1]. Such ancient and evolving coordination of molecular activities among organelles, or 'endosymbiotic synergy', underpins the core bioenergetic functions of eukaryotic cells[2]. However, the cooperating molecular partners of heterogenous origins are prone to conflicts of interests, genealogical discordance, and potential incompatibility across the species boundaries[3–7] and/or changing environment[8–14]. Therefore, the evolving synergy among endosymbiotic molecular partners can be central to climate adaptation in the rapidly changing world, yet we are merely beginning to understand the synergy behind the organismal responses to climate change, particularly in natural habitats[15].

Here we propose the 'Endosymbiotic Bioenergetic Synergy Model', which characterizes the cofunction, co-transcription, coevolution, and co-introgression among organelles involved in energy metabolism as a fundamental evolutionary step towards adaptation of eukaryotic organisms. The 'Endosymbiotic' prefix is especially relevant to this context as it reflects (1) the connection between mitonuclear coevolution theory[16–20] and the endosymbiotic theory[1,21], which delineates the origin of mitonuclear coevolution that predisposes molecular genetic constraints and opportunities for mitonuclear coevolution over space and time; (2) it incorporates multi-dimensional inter-organelle coordination beyond mitochondria and the nucleus; (3) invites integrative characterization of molecular genetic regulation[22] in eukaryotic cells underlying adaptation.

Much progress has been made in understanding the bioenergetic response to environmental variation, but the sum of individual molecular processes is insufficient to explain the collective outcome, considering the functional complexity emerged among their interactions[10,11,23]. Therefore, the emergent property in the endosymbiotic interactions remains a knowledge gap for understanding the molecular mechanisms underlying organismal climate adaptation[10,11]. The mitochondrial oxidative phosphorylation (OXPHOS) machinery at the core of animal bioenergetics is jointly encoded by nuclear and mitochondrial genomes, and coordinatively translated and maintained by mitoribosomes and cytoribosomes[24–28]. It is well known that mitochondrial biogenesis[11,25,29], ribosomal function[30,31], and OXPHOS activity[10,29,32,33]cooperate and respond to thermal changes with different sensitivity[10]. Accordingly, heat-stress often results in oxidative stress and OXPHOS disorders[34,35]. In contrast, heat acclimation is known to induce stronger ribosomal responses [36], increased protein content in Complexes I-V of OXPHOS [37], higher OXPHOS efficiency[32,33] and elevated mitochondrial biogenesis that strengthen mitochondrial energy production. Therefore, heat acclimation opens the opportunity to promote endosymbiotic efficiency and long-term heat adaptation. Remarkably, the mechanistic understanding of heat acclimation is currently missing for long-term studies of natural habitats[11]. Naturally hybridizing species that divergently adapt along a climatic gradient provide acclimation and recombination experiments to uncover such molecular genetic basis of long-term climate adaptation.

Wood warblers *Setophaga occidentalis* (SOCC, Hermit Warbler) and *S. townsendi* (STOW, Townsend's Warbler) breed in the canopy of the coniferous forests along western North America and provide a unique opportunity to determine the molecular basis of climate adaptation in a natural context[5](Fig. 1A-D). STOW breeds in the cooler and dryer inland coniferous forests of Douglas Firs, Western Hemlocks, Ponderosa Pines (Fig. 1E), while SOCC breeds in the southern warmer and humid coastal rainforests of Douglas Firs, Western Hemlocks Giant Sequoia, and Coastal Redwoods (Fig. 1F). SOCC and STOW are at the early stage of speciation with three hybrid zones, one of which is in Sister, Oregon that went through drastic environmental changes over the past two decades[38–41].

This wood warbler species complex provides a unique system to investigate the Endosymbiotic Bioenergetic Synergy Model. SOCC and STOW exhibit distinct mitochondrial haplotypes[42] with a significant signature of divergent selection in NADH dehydrogenase and ATP synthase (Fig. 1L-M)[5]. The distinct mitochondrial haplotypes coexist in ancient hybrid populations[39] and coevolve with a nuclear gene block enriched for lipid metabolism[5]. Furthermore, the mitonuclear ancestries covary with climatic variations across coastal British Columbia and Alaska, indicating climate adaptation through mitonuclear coevolution[5]. Notably, the endosymbiotic molecular interactions behind their climate adaptation remain uncharacterized.

Here we integrate blood cell bioenergetics, multiomics and life history morphometrics (Fig. 1K) to illuminate the endosymbiotic bioenergetic synergy underlying organismal climate adaptation and speciation in response to the climate changes between 1970-2000 and 2024. We ask: (1) Is there an endosymbiotic bioenergetic complex associated with divergent climate adaptation, if so, what is its composition; (2) does this complex display molecular signatures of adequate response or adaptive inertia to dramatic climate changes; (3) whether the historically warm-adapted SOCC exhibits endosymbiotic energetics of hot acclimation, featuring higher OXPHOS activities and energy capacity relative to the cold-adapted STOW; (4) whether the mismatched ancestries of endosymbiotic genes lead to compromised synergy and bioenergetics; (5) would the warm-adapted SOCC variants adaptively co-introgress across the species boundary? To infer the emergent property of these endosymbiotic molecular responses, we build a Bioenergetic Endosymbiotic Synthesis Structural Equation Model (BES-SEM) to predict the coordinated synergy of molecular activities behind organismal responses to climate change.

Results

Climate change and life history adaptation

The breeding habitats of SOCC, hybrids, and STOW partition along a climatic gradient from the historically warmer and humid SOCC temperate rainforests along coastal Oregon and California, to the cooler and drier forests of STOW in eastern Oregon, Idaho, and Montana in 1970-2000 (Fig. 1A-F). The loss of old growth forests (Fig. 1I) in concert with the rapid climate changes over the past two decades (Fig. 1G) reshaped the climatic gradient of SOCC and STOW habitats. The inland STOW breeding habitats have become drastically dryer and invertedly warmer than the SOCC

habitats (Fig. 1G). Remarkably, the temperature of the STOW habitats increased by 5.85 °C ($p < 10^{-6}$) with a reduction of monthly precipitation by 12.86 mm ($p < 10^{-4}$) in the 2024 breeding season relative to the 1970-2000 average. Severe climate changes also occurred to the hybrid habitat in Sister, Oregon with a temperature increase by 3.68 °C ($p < 10^{-7}$) and a monthly average precipitation drop by 8.24 mm ($p < 10^{-9}$) in 2024 over 1970-2000 (Fig. 1G). Despite the coastal location, SOCC habitats displayed a mild but concerning trend of a mean temperature increase by 0.42 °C ($p > 0.05$) and a mean monthly precipitation decline by 2.17 mm ($p > 0.05$) (Fig. 1G). Furthermore, the vapor pressure (VP) significantly changed in all habitats, with an average increase of 0.16 Kpa ($p < 10^{-7}$) for SOCC, 0.17 ($p < 10^{-12}$) for STOW, and 0.29 ($p < 10^{-14}$) for hybrids (Fig. 1G). These changes became particularly dramatic between 2000-2024, coincident with the massive loss (over 8 million hectares cumulatively) of old-growth western forests (Fig. 1I). These rapid and catastrophic climate changes pose challenges to climate adaptation of wildlife.

Integrating climate data and field measurements, we found that the life-history morphometrics of adult breeding warblers represents significant signatures of climate adaptation (Fig. 1J-K). The historical temperature of breeding seasons remarkably predicts the morphometric PC1 ($r = 0.30$, $p = 0.031$, Fig. 1J-K), which represents 28.2% of the total variation and reflects different beak shapes and sizes (Fig. 1J-K). Birds with bigger beaks partition to warmer breeding habitats (Fig. 1J-K), implying bigger preys in a warmer environment. PC2 represents 22.1% of the total variation, primarily reflecting wing size differences (Fig. 1K), and positively correlates with precipitation ($r = 0.30$, $p = 0.035$) of the breeding season. A larger wing surface area is known to compensate the density of humid air for aerodynamic lift[43,44], whereas a smaller wing surface in drier habitats could be adaptive to reduce water loss[45]. Remarkably, the life history morphometric axis significantly associates with historical but not recent climate conditions (Fig. 1J-K). This contrast indicates adaptive inertia or potential maladaptation, considering the inverted temperature gradient between SOCC and STOW habitats in the recent decades (Fig. 1G).

Endosymbiotic molecular basis of climate adaptation

We performed multiomic analyses and identified endosymbiotic genes at the molecular frontiers that coordinate nucleus, mitochondria, cytoribosomes, and mitoribosomes behind the observed divergent climate adaptation. Using blood cells of breeding adults, we conducted Nanopore sequencing, Illumina whole genome sequencing, and RNA-seq analyses to establish genome references and annotations, determine species-specific genotypes, and identify genes and signaling pathways that are differentially expressed among SOCC, hybrids, and STOW (see Methods). Transcriptomic analyses identified 2,037 differentially expressed genes between SOCC and STOW after ancestry normalization, with hybrids displaying intermediate expression (Fig. 2A and Fig. S1A). GO analyses (Fig. 2B) of these differential genes identify 52 key genes of three endosymbiotic modules as the top enrichment: (1) Oxidative Phosphorylation (OXPHOS) module includes 22 genes in Complexes I, III, IV, and V; (2) Hemoglobin Synthesis module contains 9 genes involved in heme synthesis within the mitochondria and hemoglobin subunits; and (3) Ribosomal Activity module consists

of 21 genes involved in mitochondrial and cytosolic ribosomes (Fig. 2A-B and Fig. S1B-D). This strong and specific enrichment highlights endosymbiotic genes at the transcriptomic frontier of divergence at the early stage of speciation.

Integrating the climate and transcriptomic data, we found that climate conditions of breeding habitats strongly explain the differential transcriptome that is enriched for endosymbiotic interactions (Fig. 2B-H). PC1 of the differential transcriptome among SOCC, STOW and hybrids is positively associated with mean gene expression levels (Fig. S1A) and significantly associated with all three climate variables after controlling for species effect (Fig. 2H, Table 1). In our regression models, both historical and present records of temperature and precipitation effectively explain the differential transcriptome better than species effects (Fig. 2H). Remarkably, the historical VP exhibits a much higher effect size ($\boldsymbol{\eta^2}$ = 0.88) than the present VP ($\boldsymbol{\eta^2}$ = 0.21) in explaining the transcriptional variation (Fig. 2H). The broad association and temporal specificity indicate transcriptomic adaptation to the historical climate with potential inertia in response to the recent dramatic climate changes.

Beyond the whole transcriptomic patterns, transcription of the three endosymbiotic genetic modules also exhibits signatures of climate adaptation (Fig. 2C-G). The transcription PC1 of endosymbiotic modules, which is positively associated with endosymbiotic gene expression (Fig. S1B-D), shows significant association with historical and present climate variables after controlling for population ancestry. Specifically, PC1 of OXPHOS gene expression is significantly associated with all three climatic variables (Fig. 2C and G). The historical VP has a remarkably greater effect size over the present VP ($\boldsymbol{\eta^2}$ = 0.7 vs. 0.26) (Fig. 2C and G; Table S1), reflecting climate niche conservatism[46] in OXPHOS functions. In addition, PC1 of OXPHOS is also significantly associated with the life history morphometric PC1 ($\boldsymbol{\eta^2}$ = 0.16, $p < 0.05$, Table S1) (Fig. 2D), which is not associated with the other two gene sets ($p > 0.05$). OXPHOS gene-expression patterns are divergent between species, where STOW shows higher expression level (Fig. 2C and Fig. S1C) but lower co-expression level among OXPHOS genes than SOCC (Fig. 2I). Hybrids display intermediate gene expression level (Fig. 2C and Fig. S1C) but the lowest co-expression among OXPHOS genes (Fig. 2I). This OXPHOS-specific phenotypic association elucidates the molecular underpinnings of the observed life history adaptation (Fig. 1J-K) and substantiates the notion that the divergent OXPHOS activities can reflect differential bioenergetics underlying alternative species-specific life history strategies [32,33,47].

Ribosomal gene expression also exhibits climate niche conservatism, as its PC1 exhibits stronger association with the historical VP ($\boldsymbol{\eta^2}$ = 0.47, $p < 10^{-5}$) than with the present VP (effect size = 0.21, $p = 0.006$) (Fig. 2G, Table S2), despite its significant association with all climate variables (Fig. 2G). In addition, the expression of hemoglobin synthesis genes is significantly predicted by the historical (effect size = 0.5, $p < 10^{-5}$) but not the present VP ($p > 0.05$) (Fig. 2F and 2G, Table S3). The repeatedly observed stronger association between historical VP and all three endosymbiotic modules indicates broad climate niche conservatism of endosymbiotic transcription. On the other hand, we also observed adaptive responses to climate change, since endosymbiotic gene expression does track recent precipitation and temperature ($p <$

0.05; Fig. 2G, Table 1). Such adaptive responses are further represented by the higher expression of endosymbiotic genes in STOWs and hybrids than SOCCs (Fig. 2C-F and Fig. S1), indicating heat acclimation of STOWs and hybrids in response to their drier and warmer habitats (Fig. 1G-H).

To sum up, the concordant associations between climatic conditions and transcription of all three endosymbiotic gene modules suggest endosymbiotic climate adaptation (Fig. 2C-G). The equivalent or greater effects of present than historical temperature and precipitation on endosymbiotic transcription (Fig. 2G) suggests adaptive transcriptional response to climate change. On the other hand, the much greater effect of the historical VP (Fig. 2G) indicates climate niche conservatism of endosymbiotic function, or adaptive inertia in complex climate response.

Bioenergetics Reveals Partial Oxidative Stress in Blood Cells

We characterized bioenergetics of blood samples to determine their metabolic state and any sign of oxidative stress during adaptation. Normal bioenergetics features a negative association between glucose and lipid (**E1**, Randle Cycle)[48], reflecting reciprocal inhibition and substrate competition between energy sources (Fig. 3A); a positive correlation between fuel availability and OXPHOS transcription (**E2**) (Fig. 3A)[49] that reflects harmonized energy metabolism; and a dynamical coupling of OXPHOS and ATP reflected by the positive correlation between ATP and OXPHOS activity (**E3**) (Fig. 3A)[22,50–52] that represents OXPHOS efficacy. Deviation in any of these features indicates cellular stress, which can be further evaluated base on the relationship between OXPHOS activity and NADPH/$NADP^+$ ratio[53–56]. When OXPHOS operates under oxidative stress (Fig. 3A) (**E'**), the NADPH-dependent antioxidant defense is frequently compromised and leads to a negative association between OXPHOS and NADPH/$NADP^+$ ratio[53,55].

We observed the negatively associated FFA and glucose[48] (Fig. 3B) (**E1**) and the positively correlated OXPHOS gene expression with energy sources (glucose and TAG) (Fig. 3B; Table S4, S5) (**E2**), consistent with partially normal metabolism. However, the absence of a positive correlation between OXPHOS transcription and ATP production (**E3**) reflects potential OXPHOS inefficiency: the expression of NDUFV2 (encoding a core subunit of complex I) is marginally (Table S6, $p = 0.02$, $p_{FDR_adjusted} = 0.39$) negatively correlated with the ATP level (Fig. 3B) (**E3**), and none of other OXPHOS genes is correlated with ATP ($p > 0.05$). Loss of a positive link between OXPHOS transcription and ATP production indicates potential disordered OXPHOS biogenesis and/or functions. Such OXPHOS disorders are frequently observed in cells under heat stress[34,57]due to asynchronized ribosomal[30,31] and OXPHOS responses to increased temperature[10,29,33,58]that disrupt endosymbiotic synergy for cellular energetics[10].

Furthermore, we observed a negative correlation between NADPH/$NADP^+$ ratio and OXPHOS transcription (Fig. 3B) **(E')** that indicates oxidative stress[53–56]. NADPH is consumed for antioxidative protection, sustaining the OXPHOS operation despite metabolic oxidation[54,55]. In our warbler blood samples, significant negative correlations are broadly detected between the NADPH/$NADP^+$ ratio and OXPHOS genes involved in the Complexes I, IV and V (Fig. 3B; Table S7) (**E'**). When cells are under oxidative stress, electron leakage from Complex I incurs a buildup of reactive oxygen species that

require antioxidant defense for OXPHOS to further operate at the cost of NADPH[59], resulting in a negative correlation between the OXPHOS activity (reflected in OXPHOS gene expression level) and NADPH/$NADP^+$ ratio.

Integrating metabolic and multiomics data derived from the same blood samples, we identified the strongly climate-associated endosymbiotic transcription behind energetic adaptation to climatic conditions. These molecular insights reflect both climate adaptation (Fig. 2C-H and Fig. 3A, E1-E2) and adaptative inertia that are represented by OXPHOS inefficiency and oxidative stress in the blood cells.

Bioenergetic difference between species

Consistent with the heat acclimation prediction[11], the historically warm-adapted SOCC exhibits the best energy capacity over STOW and hybrids ($p < 0.05$), displaying higher ATP and energy source ATP conversion in the form of free fatty acid (FFA) and triglyceride (TAG) (Fig. 3C). Moreover, SOCC blood cells exhibited significantly greater surface areas of the mitochondria inner membrane than STOW (mean difference = 1.01, 95% CI: 0.51 to 1.52, confocal nested design: 3 individuals per species, 30 randomly sampled blood cells per individual, Fig 3D), concurring with the stronger SOCC energy capacity (Fig. 3C). These results support the bioenergetic continuity of heat acclimation and heat adaptation[11], with the historically warm-adapted SOCC displaying higher energy capacity and mitochondria inner membrane.

Endosymbiotic co-expression network (ECN) reflects strong molecular synergy

To understand the emergent properties of endosymbiotic bioenergetic activity, we built ECNs for each warbler population (Fig. 4A-C). Molecular synergy between each pair of endosymbiotic genes is identified as a weighted edge of ECN (Fig. 4B). An edge is formed if the absolute transcriptional correlation coefficient of a pair of genes is significantly greater than the transcriptomic background (Fig. 4C). The weight of each edge is the absolute value of the correlation coefficient. The full ECNs in all three warbler populations (Fig. 4C-D) display significantly greater co-expression synergy than randomly sampled equal-sized networks (Fig. 4D, $p < 10^{-15}$). Such transcriptional synergy of endosymbiotic genes is in line with their functional interactions[23,60–62].

Consistent with the heat acclimation prediction and bioenergetics measurements, the historically warm-adapted SOCC has the most synergized and efficient endosymbiotic machinery. SOCC has the highest ECN density that reflects remarkably stronger endosymbiotic synergy over STOW and hybrids ($p < 10^{-15}$) (Fig. 4A-D). Such synergy facilitates better coordination and efficiency of metabolism that are reflected by the higher energy capacity in SOCC blood cells (Fig. 3C), despite their lower endosymbiotic gene expression than STOW and hybrids ($p < 0.05$) (Fig. 2C-E). The hybrid ECN has significantly fewer edges thus lower synergy than SOCC or STOW ($p < 10^{-15}$), suggesting hybrid incompatibility among mismatched endosymbiotic ancestries as predicted by the Endosymbiotic Snowball Effect[63].

The synergy within each of the three endosymbiotic modules (Fig. 4D) is consistent with their known functional interdependence. The Ribosomal Module has the highest synergy over the Hemoglobin Synthesis and OXPHOS Modules (Fig. 4D), reflecting the dependency of mito-ribosomes biogenesis on cyto-ribosomes[64]. The historically warm-adapted SOCC has significantly higher synergy within the Ribosomal

and OXPHOS Modules than STOW and hybrids ($p < 10^{-15}$) (Fig. 4D), with hybrids showing the lowest synergy of OXPHOS ($p < 10^{-14}$). This result indicates greater functional integration within OXPHOS and ribosome in the SOCC population. In contrast, STOW has the highest synergy within the Hemoglobin Synthesis Module than SOCC and hybrids ($p < 10^{-15}$), which show similar synergy. The outstanding synergy of Hemoglobin Synthesis module in STOW is reminiscent of high-altitude adaptation, as STOW breeds at significantly higher elevation (Fig. 1A) that requires greater hemoglobin function to strengthen oxygen transport[65].

SOCC also displays the highest synergy across functional modules. The Ribosomal Module is the hub (Fig. 4E) of endosymbiotic synergy, as this module tightly synergizes with the Hemoglobin Synthesis and OXPHOS Modules in SOCC ($p < 0.05$) and hybrids ($p < 0.05$) (Fig. 4D-E). Such hub status of the Ribosomal Module (Fig. 4D-E) is consistent with its functions, since mitoribosomes translate the core subunits of OXPHOS, and the biogenesis of mitoribosomes and hemoglobin relies on cytoribosomes[64]. On the other hand, all three modules show similar ($p > 0.05$) hub scores in the ECN of STOW (Fig. 4E). This difference could be related to greater hemoglobin centrality in low-oxygen habitat of STOW (Fig. 1A) where oxygen transportation could be central in the coordination of OXPHOS biogenesis and energy production.

The co-expression synergy between modules is the highest in SOCC, followed by STOW then hybrids (Fig. 4D), suggesting stronger endosymbiotic functional integration in the historically warm-adapted SOCC. Collectively, the species differences in endosymbiotic synergy are consistent with the heat acclimation prediction, where SOCC has the highest endosymbiotic synergy (Fig. 4), bioenergetic efficiency and capacity (Fig. 3).

Introgression across species boundaries reshapes endosymbiotic functions

Since the SOCC ECN has superior synergy and bioenergetic capacity, we hypothesize that the introgression of historically warm-adapted SOCC endosymbiotic variants can be selected by climate change in the hybrid and STOW habitats (Fig. 1G-H). Indeed, our Bayesian Genomic Cline analysis on the whole genome sequencing data suggests the excessive SOCC-biased introgression in endosymbiotic genes (Fig. 5A and D-G), reflected by the significantly negative center (α) and rate (ß) parameters (Fig. 5F-G). Collectively, SOCC endosymbiotic genetic complexes are more efficient and selected to penetrate species boundaries, as they exhibit higher endosymbiotic synergy (Fig. 4D) and total energy capacity (Fig. 3C-D).

On the other hand, hybridization has a negative effect on endosymbiotic adaptation, as genetically discordant hybrids (Fig. 5C) have significantly lower endosymbiotic synergy (Fig. 4) and total energy capacity (Fig. 3C) than parental species. The incompatibility among endosymbiotic genes incurs synergistic selection against hybrids, contributing to speciation[63]On the other hand, the synergistic selection of genetic concordance across unlinked genomic regions can be counteracted by gene flow[66]. Depending on the tension between synergistic selection and gene flow, adaptive endosymbiotic introgression can penetrate the species boundary when an asymmetric selection favoring the historically warm-adapted SOCC variants is strengthened by

climate changes. Remarkably, we uncovered the temporal resolution of these conflicting yet entangled evolutionary forces acting on the endosymbiotic genetic complexes across the species boundary.

Endosymbiotic synergy in response to hybridization & climate change

To understand the effect of climate change and hybridization on endosymbiotic synergy and its implication for bioenergetics and organismal life history, we built a Structural Equation Model (SEM) for Bioenergetic Endosymbiotic Synthesis (BES) with 10,000 simulated ECNs (see Methods) based on our field data (Fig. 1). This comprehensive predicative framework integrates natural genetic recombination, variations in endosymbiotic molecular bioenergetics, and climatic heterogeneity across the allopatric parental range and hybrid zones (Fig. 1 and Fig. 5H-J). BES-SEM reveals alternative endosymbiotic molecular strategies for bioenergetic adaptation to climate change (Fig. 5J; Table S1) that significantly affects life history morphometrics (Fig. 5J, absolute effect size > 0.14, $p < 0.05$).

BES-SEM suggests that the endosymbiotic genetic discordance (Fig. 5H) along with hybridization compromises endosymbiotic synergy (Fig. 5J, effect size = -0.63, $p < 0.05$). The latter in turn significantly and positively (Fig. 5J, effect size = 0.19, $p < 0.05$) predicts the total energy capacity of blood cells (Fig. 5I). Consistently, hybrids display higher genetic discordance among endosymbiotic genes ($p < 0.0001$) than parental species (Fig. 5A-C) with the lowest endosymbiotic synergy (Fig. 4) and blood energetics (Fig. 3). Such integrated results provide direct support to the 'Endosymbiotic Snowball Effect' [63], which predicts that the mismatched ancestry in the endosymbiotic genes reduces hybrid fitness. In contrast, the heterozygosity within endosymbiotic genes has an indirect positive effect on endosymbiotic synergy via its significantly negative effect on the latent factor η_3 (Fig. 5J, effect size = -0.4, $p < 0.05$). The latent factor η_3 synthesizes the effects of discordance and heterozygosity, and negatively affects endosymbiotic synergy (Fig. 5J, effect size = -0.63, $p < 0.05$). The positive effect of heterozygosity suggests that the effect of recessive deleterious alleles can be masked in heterozygous state, which maintains endosymbiotic synergy that is simultaneously disrupted by between-loci incompatibility.

Furthermore, BES-SEM identifies a negative effect of STOW ancestry on the endosymbiotic synergy that is strongly contextualized in climate change (Fig. 5J). Specifically, the latent variable η_2 positively indicated by STOW ancestry (Fig. 5J, effect size = 0.94, $p < 0.05$) has a significant negative effect on endosymbiotic synergy (Fig. 5J, effect size = -0.40, $p < 0.05$). This observation suggests that STOW alleles tend to have recessive deleterious effects on endosymbiotic synergy, considering that the heterozygosity within endosymbiotic genes is positively associated with synergy (Fig. 5J). The negative effect of STOW ancestry on endosymbiotic synergy is strongly associated with climate changes (Fig. 5H and J, effect size = 0.82, $p < 0.05$), as the STOW habitats have experienced more dramatic changes than the SOCC habitats (Fig. 1G-H). Endosymbiotic synergy could collapse in the face of rapid climate change as the cooperating modules respond with different environmental sensitivity (Sokolova, 2023).

In contrast, the blood cells of STOW exhibit an alternative bioenergetic strategy via elevated endosymbiotic transcription as opposed to synergy (Fig. 5J, effect size = -

385 0.18, $p < 0.05$). Like endosymbiotic synergy (see above), elevated endosymbiotic
386 transcription also can promote energy capacity of the blood cells (Fig. 5J, effect size =
387 0.18, $p < 0.05$). In particular, the latent variable η_2, which is positively indicated by the
388 STOW ancestry, has a strong positive effect on endosymbiotic transcription (effect size
389 = 0.81, $p < 0.05$). Together, BES-SEM reveals alternative endosymbiotic strategies
390 behind organismal responses to climate change from ancestries adapted to divergent
391 climatic conditions. The alternative adaptive responses can be simultaneously
392 hampered and assisted by hybridization.

Discussion

Endosymbiotic Bioenergetic Synergy Model

Our multi-omics, blood cell metabolism, and life history morphometric analyses support the 'Endosymbiotic Bioenergetic Synergy Model', in which the coordinated endosymbiotic molecular genetic cofunction, co-transcription, coevolution, and co-introgression behind energy metabolism are fundamental to adaptation of eukaryotic organisms. In particular, we uncover an endosymbiotic bioenergetic complex that is the most differentially transcribed between the divergently climate-adapted wood warbler species at the early stage of speciation. The transcription levels of these endosymbiotic bioenergetic genes are strongly linked to the breeding climatic conditions after controlling for species effects (Fig. 2). This set of endosymbiotic bioenergetic genes exhibit significant transcription synergy (Fig. 4) that positively predicts blood cell energy capacity (Fig. 3C and Fig. 5J). This synergy is significantly associated with life history morphometrics (Fig. 5J). Collectively, multiple lines of independent evidence converge and suggest the fundamental role of endosymbiotic bioenergetics in organismal climate adaptation.

Synergistic insights from this wood warbler system inspires the development of a new verbal model of eukaryotic adaptation: 'Endosymbiotic Bioenergetic Synergy Model'. This model characterizes the coordination of molecular activities among organelles involved in energy metabolism as a fundamental evolutionary step towards adaptation in eukaryotic organisms. This model connects the emerging evidence in which mitonuclear coevolution contributes to environmental adaptation[13,14,18,67–69], and further substantiates the understanding of eukaryotic bioenergetics by integrating the origin, organellar diversity, and molecular genetic integration of coordinated endosymbiotic evolution.

For the model to effectively capture the regularity underlying eukaryotic adaptation, here we propose to consider 'endosymbiotic' beyond the 'mitonuclear' prefix. First, the 'endosymbiotic' prefix connects mitonuclear coevolution literature with the Endosymbiotic Theory[1,21] of eukaryotic origin. The term 'endosymbiotic synergy' highlights the heterogenous evolutionary origins forming a 'unified' symbiotic evolutionary trajectory in the origin of the intracellular coevolution. The endosymbiotic fusion predisposed the contemporary coevolutionary dynamics via the partial autonomy[70], conflicts [20], compensation[71], and gene transfers[72] among organelles.

Second, this 'endosymbiotic' prefix encompasses key organellar activities such as mitoribosome and cytoribosome that tend to be overlooked in the mitonuclear coevolution. The assembly of OXPHOS machinery requires the precise coordination between mitoribosomes and cytoribosomes[73], as a portion of the OXPHOS subunits are encoded as mtDNA and translated by mitoribosomes[74,75], while majority of the subunits are encoded in the nuclear genome and translated by the cytoribosomes[73]. Indeed, we found strong and dense co-expression connections between cytoribosomes and mitoribosmes; and the ribosomal genes are hubs in the endosymbiotic co-transcriptional networks (Fig. 4 D).

Furthermore, this 'endosymbiotic' prefix enables multi-ways integration of endosymbiotic organelles besides mitochondria, such as chloroplasts and

kleptosomes[76] in eukaryotic adaption. Finally, the 'endosymbiotic' prefix invites integrative synthesis of molecular genetic synergy beyond genomic coevolution. For instance, the encoding, transcription, and translation of mitoribosomes require molecular genetic synergy among the nucleus, mitochondria, and cytoribosomes[64]. BES-SEM (Fig. 5) effectively integrate biological hierarchies with extrinsic environmental variations and can be widely applied to other eukaryotic systems to elucidate endosymbiotic bioenergetic synergy behind adaptation and speciation. Collectively, 'Endosymbiotic Bioenergetic Synergy Model' has a potential of opening a new era of inter-organelle coevolution.

Climate Adaptation In response to the dramatic climate changes in the breeding habitats over the recent two decades (Fig. 1), warbler blood cells display signatures of adaptation but also signs of oxidative stress and bioenergetic inefficiency (Fig. 3). Specifically, all breeding habitats experienced higher vapor pressure and temperature with decreased precipitation (Fig. 1). These changes were especially extreme in the habitats of STOW and hybrids (Fig. 1). The latter two populations have significantly inferior bioenergetics (Fig. 3) and endosymbiotic synergy (Fig. 4) than SOCC. Consequently, a less efficient alternative strategy emerged in STOW in the form of elevated antioxidant defense (Fig 3) and endosymbiotic transcription (Fig. 2-3) to maintain bioenergetics (Fig. 5J). In contrast, the historically warm-adapted SOCC strategy with low endosymbiotic transcription (Fig. 2) and high synergy (Fig. 4) appear energetically superior with greater total energy capacity (Fig. 3). The STOW strategy could yet to undergo heat acclimation and evolution towards heat adaptation.

The observed adaptive inertia (Fig. 1 J, 2, Table 1, S1-S3) is potentially explained by compromised endosymbiotic bioenergetic synergy in populations breeding in drastically altered climatic conditions. Signatures of adaptive inertia were observed in endosymbiotic transcription (Table 1) and life history morphometrics, where the historical climate exhibited stronger association than the present climate. Climatic adaptive inertia reflects climate niche conservatism as a tendency of populations to retain ancestral climatic tolerances over generations [46,77]. Such inertia is most strongly reflected in the endosymbiotic transcriptional tracking of vapor pressure (Table 1), which is a more complex climate variable than temperature and precipitation thus potentially requiring greater endosymbiotic fine-tuning.

Although climate adaptation is merely inferred through the strong and significant climate association with endosymbiotic transcription (Table 1) and life history morphometrics, future mechanistic investigation could be confirmative. Despite that conducting a mitonuclear recombination or transgenic experiment as previously done in *Drosophila*[14] is practically unfeasible for the focal terrestrial vertebrate system, this study leveraged the abundance of natural recombinants in a hybrid zone, where the endosymbiotic bioenergetic genetic variants were recombined over generations of hybridization (Fig. 1 & 5). We discovered that the endosymbiotic genetic discordance in hybrids corresponds with reduced endosymbiotic co-expression synergy and total energy capacity (Fig. 5 I).

Speciation Progression: The Tension of Incompatibility & Introgression

Hybridization acts as a double-edged sword to climate adaptation. On one hand, it leads to endosymbiotic incompatibility (Fig. 5H), which increases endosymbiotic discordance (Fig. 5C), compromises endosymbiotic synergy (Fig. 4, Fig. 5C, H), and hampers bioenergetic capacity (Fig. 3C; Fig. 5H-I and J), thus impedes climate adaptation. On the other hand, hybridization enables the adaptive introgression of the historically warm-adapted SOCC variants (Fig. 5F-G), which could help rescue the STOW population confronting rapid warming (Fig. 5I) thus facilitates climate adaptation. Heterozygosity within the endosymbiotic bioenergetic complex indeed promotes endosymbiotic synergy and bioenergetics despite the negative effect of genomic heterozygosity (Fig. 5J). Remarkably, we observed contrasting effects of hybridization that shape endosymbiotic bioenergetic adaptation across the species boundary of SOCC and STOW.

The speciation progression depends on the tension of adaptive introgression and endosymbiotic incompatibility in the context of climate change. The hybrid zone in Sisters OR may become narrower due to the reduced hybrid fitness that results from the compromised endosymbiotic synergy (Fig. 5F). The hybrid fitness loss can be magnified by the rapidly changing climate in the hybrid habitat (Fig. 1G-H). If so, speciation would unfold. Simultaneously, the species boundary may shift towards STOW direction as the warm-adapted SOCC endosymbiotic variants asymmetrically penetrate the species boundary (Fig. 5F). Although the adaptive introgression can encounter resistance by the endosymbiotic incompatibility, the SOCC-biased dominance (Fig. 5F) weakens the resistance. Such asymmetrical introgression of endosymbiotic alleles consequently slows down speciation. Collectively, the emergent effect of climate change on speciation resides in the tension of endosymbiotic incompatibility and introgression.

Conclusion

The catastrophic climate changes in the North American temperate rainforest (Fig. 1G) have significant impacts on organismal bioenergetics, life history, and the species boundary. This study of a species complex of the forest canopy endotherms inspires the 'Endosymbiotic Bioenergetic Synergy Model' by characterizing the highly synergized co-transcription, coevolution, and co-introgression among organelles orchestrating bioenergetics behind climate adaptation. In addition, we identified signatures of adaptive inertia especially in populations that have experienced dramatic climate changes, and this inertia can be partially alleviated by the penetration of warm-adapted endosymbiotic genetic variants through the nascent and evolving species boundary.

Materials and Methods

Sampling

We conducted field sampling during the breeding season (June-July) of 2024 by mist-netting with an audio lure[39–41] in the breeding territories of SOCC, STOW, and a hybrid zone in Sisters, OR (Fig. 1). Upon capturing each breeding adult, we collected a blood sample then conducted life history morphometric measurements including beak morphology: beak depth, beak width, the distance between the anterior rim of the nares to the tip of the beaks (nares-to-tip), and culmen length, as well as wing chord, the tip of the longest primary to the longest secondary wing feather, tarsus length, and body weight. Meanwhile, blood cells and serum were immediately separated (1,000g for 1min) upon collection for snap-freezing, DNA/RNA Shield (Zymo, R1100-50) storage, or cross-linking (10min in 1% PFA) followed by quenching, PBS washes and snap-freezing. Fresh-sample-freezing and crosslinking were completed and started, respectively, within 3 minutes after collection for sample integrity.

Climate adaptation

To compare the historical versus recent climatic conditions of SOCC, STOW, and hybrid habitats (Fig. 1A), we compared mean temperature (°C), monthly precipitation (mm), and vapor pressure (kPa) of breeding seasons (June and July) of 1970-2000 and 2024, when sampling was conducted in the present study. We acquired the historical climate data from worldclim2 (https://www.worldclim.org/data)[78] and the 2024 data from National Aeronautics and Space Administration (NASA) Langley Research Center's Prediction of Worldwide Energy Resources (POWER) Project (https://power.larc.nasa.gov/api/temporal/daily/point) with GPS coordinates of the sampling sites (Fig. 1A-D). To gain yearly average of June-July climate conditions, we downloaded NASA historical climate data of the same variables between 1981-2024. To understand the extent of climate changes along the western forest, we downloaded data of yearly forest cover loss (in hectares) in CA, OR, WA, and ID from Global Forest Watch (https://www.globalforestwatch.org)[79]with the *jsonlite* (Ooms 2014) and *httr*[80]packages in R.

To investigate the three climatic variables in each sampling site, we conducted paired t test. To examine local climatic adaptation of the wood warblers, we conducted correlation tests between the three climatic variables from 1970-2000 and life history morphometrics of breeding adults. In particular, we measured beak shapes: beak depth, beak width, the distance between the anterior rim of the nostril to beak tip (nare.to.tip), and exposed culmen length (Fig. 1K). We also measured body weight, tarsus length, wing chord, the distance between the longest secondary and primary feather (primary.secondary) (Fig. 1K). We conducted reduction of dimensions with centered and scaled principal component analysis (PCA) prior to correlation tests with the climatic variables.

Mitochondrial genetics and protein structure

To understand mitochondrial divergence, we acquired genomic sequences (N = 20 SOCC and N = 20 STOW) of mitochondrial ND2 gene[42] from Genbank[81]). The sequences were aligned with *msa* function under the *msa* package[82] in R with the following setting: ‘method = "Muscle" (Edgar 2004), gapOpening = 20, gapExtension =

10'. Then, we computed the distance matrix with *dist.ml* with *phangorn* package[83] in R, to fit an initial neighbor joining tree with *nj* with ape[83]. Then we searched for the maximum likelihood phylogeny under the GTR+G+I model with *pml* function in *phangorn*[83]

To understand the potential structural difference in the mitochondrial energetic proteins, we downloaded *.pdb* files of ND2 and ATP synthase subunit A from AlphaFold[84].Per-residue root mean square deviation (RMSD) between SOCC and STOW ND2 and ATP synthase subunit A were calculated with ChimeraX-1.11.1[85].

Nanopore sequencing of SOCC and STOW reference genomes

Blood cell DNA from adult males was extracted with Blood & Cell Culture DNA Kit (Qiagen), quantified with Qubit dsDNA HS Assay Kit (Thermo Fisher Scientific) and integrity-examined with Genomic DNA HS ScreenTape (Agilent) according to manufacturer's protocols. 1 µg of high-quality gDNA was used to generate libraries with Ligation sequencing DNA V14 kit (Nanopore, SQK-LSK114) that were sequenced ~ 50X on PromethION Flow Cells at Jacobs School of Medicine and Biomedical Sciences of State University of New York, Buffalo.

We assembled SOCC and STOW references using Nanopore sequencing that were annotated with a combination of our RNA-seq data (see below) and the songbird protein homology database. Nanopore reads were trimmed with NanoFilt (-q 10, -l 1000)[86] with adaptors removed by porechop. Then we conducted *de novo* assembly with FLYE[87] and polished the assembly with MEDKA[88] and model "r94_prom_sup_g507". The polished genome was scaffolded with RagTag[89] and the homologous chromosomes were matched to zebra finch reference (GCF_048771995.1.fa). Non-chromosomal contigs were filtered out with seqkit. Repeats were soft-masked with RepeatModeler 2.0.7[90]. RNA-seq reads were mapped to the repeat-masked genome assembly with HISAT2 (Kim et al. 2019). Annotation was performed by Braker3[91]with RNA-seq alignment to the newly assembled genome (--bam) and protein homology database (--prot_seq) of all songbirds. Gene names of the annotation were extracted with blastp[92] with the following specification: -db uniport and -evalue 1e-5.

The resulting reference genomes are of high quality and continuity: the SOCC assembly has BUSCO = 99.5%, N50 = 73,084,269, L50 = 6; and the STOW assembly has BUSCO = 99.5%, N50 = 73,854,319, L50 = 6.

Whole Genome Sequencing (WGS)

Blood cell DNA was extracted and quantified with Qubit dsDNA HS Assay Kit (Thermo Fisher Scientific) and integrity-examined with Genomic DNA HS ScreenTape (Agilent). 100ng gDNA was used to generate libraries that were sequenced on NovaSeq X (Illumina) by 150 bp paired-end sequencing for 17 SOCC, 10 STOW, and 12 hybrid warblers.

WGS reads were trimmed with trimmomatic-0.39[93]and aligned to the nanopore genome assembly with bwa[94]. Variant calling was conducted with *bcftools*[95]*mpileup* function with the following specifications: -q 20 -Q 20 -C 50 -Ou. We computed the SNP-based F_{ST} between SOCC and STOW with vcftools[95]. To acquire ancestry-informative SNPs, we extracted the genomic positions with $F_{ST} > 0.8$.

Parental species differential gene expression

Blood cell RNA was extracted with RNeasy Plus Micro Kit and on-column DNase treatment then quantified according to manufacturer's protocols. RNA integrity was confirmed with High Sensitivity RNA ScreenTape (Agilent), and 25 ng high-integrity RNA was used to generate RNA-seq libraries with Illumina Stranded mRNA Prep. Libraries were sequenced on NovaSeq X (Illumina) by 150 bp paired-end sequencing for 15 SOCC, 9 STOW and 12 hybrid warblers. Differential genes were determined following our previously published procedures with minor modifications[96,97]. Briefly, using cutadapt[98], we performed quality trimming, and poly A and adapter trimming. The trimmed read pairs were mapped with HISAT2 (--sensitive --no-mixed --no-discordant) to the SOCC or STOW reference for high quality alignments, which were counted for exons of annotated genes using featureCounts (strand -s 2)[99]. DESeq2 package[100]in R was used to identify differentially expressed genes (FDR<0.05, lfcShrink type=ashr).

Hybrid gene expression and Gene Ontology Analysis

To determine heterogeneous ancestry representation in hybrid transcriptomes, we generated individual-specific mosaic parental reference to quantify hybrid gene expression. In particular, we aligned the RNA-seq and WGS reads from each hybrid individual to both parental reference genomes, using HISAT2 and bwa. For each gene region (with 1Kb flanking around the start and end of the gene), we calculated its sequence alignment scores to both STOW and SOCC reference with the WGS data from each of the same sample. We then used the reference of the higher score to quantify gene expression counts. This WGS-guided gene-specific reference provides independent ancestry information for hybrid RNA-seq alignment and quantification, which were further processed following the same procedure as parental species above.

Gene Ontology analysis on the divergently expressed genes between the parental species was conducted with goProfiler[101] and *tguttata* genes network. We extracted the genes corresponding to the significant GO terms for downstream analyses.

Climatic adaptation in metabolic transcription

To understand transcriptive adaptation to climatic conditions, we examined the climate association with gene expression in the enriched molecular clusters (OXPHOS, Ribosomal, and Hemoglobin Synthesis Pathways). We first conducted reduction of dimensions with centered and scaled principal component analyses of the gene expression profiles of each genetic cluster. To investigate climate adaptation and the potential adaptive inertia, we conducted regression modeling in which the response variables were PC1 of differential transcriptome, and the predicting variables were species (SOCC, STOW, vs hybrids), historical (1970-2000) and present (2024) climate (temperature, precipitation, and vapor pressure). We examined the association between mean gene expression level and transcription PC1 with a linear regression to determine the transcription orientation of the PC1. A significant transcriptional association with local climatic variation suggests climate adaptation. The time gap between the climate sampling is around 10 generations when rapid climate change occurred (Fig. 1). A rapid climate adaptive response would predict strong transcriptional association with recent

climate. In contrast, an adaptive inertia[102] or climatic niche conservatism[46] to recent climate change predicts greater effect size of historical climate than present climate.

To accurately and effectively represent the climatic condition of each bird's breeding habitat, we extracted the June-July air temperature (C°) at 2 meters above the Earth's surface, monthly precipitation (mm), and vapor pressure (kPa) at the GPS coordinate where each sample was collected. We fitted a regression model for each climate variable to compare the effects of historical versus present climatic conditions while controlling for species effect. To understand the range of effects of each historical and present climate variables, we conducted 1000 bootstrap sampling of the full dataset to generate the bootstrap distribution of effect size for each climate variable.

Endosymbiotic Co-expression Network (ECN)

To examine the synergy among endosymbiotic genes, we constructed a co-expression network among genes in the three endosymbiotic modules (see **Gene Ontology Analysis**) in each population (SOCC, STOW, or hybrid). Each node represents a gene. An edge emerges if the pair of genes are significantly co-expressed in each population. The edge weight is the absolute co-expression correlation coefficient between the two genes in the designated population. The 95th percentile of the absolute correlation coefficients of all pairwise co-expressions in the transcriptome were used as the threshold for significant co-expression. If the expression correlation coefficient between a pair of genes was greater than that threshold in a population, an edge would form between this pair of gene nodes. The significantly positive and negative correlations are not differentiated in the network, which reflects the strength of pairwise co-transcription. The weight of the edge is the absolute value of the correlation coefficient. All pairwise co-expression associations of the 52 genes from the three functional modules (see above) were evaluated to generate the full Endosymbiotic Co-expression Network (ECN) of each population.

To determine the synergy among endosymbiotic genes in each population, we quantified edge density[103] and global efficiency[104] of each ECN with *igraph*[105] in R. Furthermore, we evaluated the synergy within each functional module and sub-module. For each network, module, or sub-module of a population (SOCC, STOW, or hybrid), we randomly generated 10,000 subsamples consisting ¾ of the nodes. To test whether the ECN was significantly different from random co-expression, we generated a null distribution by randomly sampling 10,000 equal-sized co-expression networks from the transcriptome. We then conducted one-way ANOVA followed by *post hoc* tests with Bonferroni multiple hypotheses correction[106] to compare endosymbiotic synergy of ECNs among different populations relative to the null distribution.

To understand the relative centrality of the three functional modules, we calculated the mean weighted centrality hub score[107] of vertices within each module. The module with greatest the hub score is the central connector of ECN.

Hybrid genomics and endosymbiotic genetics

The genomic ancestry of each individual is calculated with ancestry informative SNPs (F_{ST} > 0.8 between SOCC and STOW)[5]. SNP-calling was conducted with bcftools (Danecek et al. 2021). F_{ST} was calculated with vcftools[108] excluding sites with low quality scores and depth (QUAL < 20, DP <10) or missing > 30% data. Homozygous SOCC,

heterozygous and STOW genotypes were represented with scores 0, 0.5, and 1, respectively. Genomic hybrid index (HI) for each individual is the average of all the ancestry-informative SNPs. Divergent endosymbiotic genetic positions were extracted as SNPs within the 52 divergently expressing endosymbiotic genes (see **Gene Ontology Analysis section**) with maximum missing genotype being 30% across all individuals, with the mean HI difference of at least 0.3 between SOCC and STOW. The standard deviation of HI across the divergent endosymbiotic genetic positions provides a proxy of 'endosymbiotic genetic discordance' (EGD). We tested whether EGD was significantly different between SOCC, STOW, and hybrids with ANOVA followed by TukeyHSD *post hoc* tests. In addition, we estimated individual heterozygosity both for the ancestry informative as well as for the endosymbiotic genetic positions. Heterozygosity is calculated as the fraction of heterozygous sites of total sites.

To understand the introgression of endosymbiotic genes relative to the genomic background, we conducted Bayesian genomic cline analyses[109]. Specifically, we examined the deviation of endosymbiotic genetic HI from genomic HI, by estimating two parameters: α and ß that represent the direction and the rate of introgression, respectively. While 0 values of α and ß represent neutral diffusion, a significantly positive vs negative $\alpha(s)$ reflect STOW vs SOCC-biased introgression. A significantly positive ß implies divergent selection, whereas a significantly negative ß represents excessive introgression.

Blood cell bioenergetics

To evaluate the bioenergetic conditions of blood cells, we integrated transcriptomics with energy metabolism analyses. We examined three expectations of normal bioenergetics based on the literature: (E1) signature of Randle Cycle, which expects a negative correlation of glucose level and Triglyceride (TAG); (E2) fuel availability whether through glycolysis versus lipolysis should be positively associated with OXPHOS activity; (E3) OXPHOS homeostasis, reflected as the dynamical coupling of OXPHOS gene expression and ATP level[22,52]. Cell stress is indicated if one or more of E1-E3 was rejected. If so, we evaluated a biochemical indicator of oxidative stress (E') as indicated by the association of NADPH/$NADP^+$ ratio and OXPHOS gene expression. Under oxidative stress, the electron transport chain activity leads to ROS leakage, and more antioxidant defense and NADPH consumption, resulting in a negative association of NADPH/$NADP^+$ ratio and OXPHOS activity indicated by OXPHOS gene expression level.

To investigate the four bioenergetic expectations (E1-E', Fig. 3), we quantified the following metabolites: (1) glucose levels, (2) TAG, (3) FFA, (4) ATP, and (5) NADPH/NADP+ ratio in blood cells of for 5 SOCC, 6 STOW and 11 hybrid breeding warblers. The association analyses between blood biochemical profiles and OXPHOS gene expression were performed using the same blood samples. False Discovery Rate (FDR) correction[110] is applied for multiple hypothesis testing correction of the association of metabolites with OXPHOS gene expression. These commercial kits were used according to manufacturers' protocols to quantify the ordered metabolites above: Autokit Glucose (FUJIFILM, 997-03001), Triglyceride-GloTM Assay, HR Series NEFA-HR-2 kit (FUJIFILM), CellTiter-Glo® 2.0 Assay and NADP/NADPH-GloTM Assay.

To compare the energetics among species, we derived the metric of 'Total Energy Capacity', which is the weighted average of scaled ATP production and energy source. The energy source is approximated as the weighted (based on per substrate ATP conversion) average of glucose, FFA, and TAG in the ratio of 1: 3.5: 11, reflecting the total ATP production capacity.

Immunochemistry, imaging and quantification

The crosslinked, snap-frozen blood cells were used for immunochemistry following a published protocol[97]with a COX IV primary antibody (ab16056) at 1:500 and secondary antibodies at 1:1,000 to visualize the mitochondria inner membrane. DAPI was used as a counterstain of nuclei. Confocal images of separate single cells were taken for maximum-intensity z-series projections, and the total mitochondria inner membrane area was quantified using the Mitochondria Analyzer plugin in FIJI (threshold = 30)[111] for each cell. The mitochondria inner membrane area of each animal was calculated as the average of 30 randomly imaged blood cells for each of the three biological replicates. Statistical significance was determined by nested Bootstrapping tests.

Climate change scores

We computed the climatic deviation (**δ**) among three climate variables, where the deviation for each climate variable is the difference between 2024 and 1970-2000 average. For instance:

$$\delta_{prec} = prec_{2024} - prec_{1970-2000}$$

To evaluate the effect of climate change, we transformed the climate deviation score into the Scaled Climate Change Score (***p***), which is the subsample average of δ_i for each time, and the location is scaled relative to the all-time maximum (δ_{max}) and minimum (δ_{min}) change of the respective climate variable:

$$\boldsymbol{p} = \frac{\delta_i - \delta_{min}}{\delta_{max} - \delta_{min}}$$

The Scaled Climate Change Scores for temperature, precipitation, and vapor pressure are respectively denoted as p_T, p_P, and p_V.

Simulated endosymbiotic synergetic evolution

To understand the evolution of endosymbiotic synergy in bioenergetic responses to climate change and hybridization, we simulated 10,000 ECNs in an integrative predictive framework (see below). To best leverage the natural variation among SOCC, STOW, and hybrids, we mixed the samples from all three populations to form a virtual panmictic population. In each iteration, we randomly sampled 16 out of 39 individuals from the virtual panmictic population to compute an ECN. We estimated the endosymbiotic synergy as the global efficiency of the ECN. Simultaneously, for each ECN, we recorded the corresponding average scaled climate change scores, genomic hybrid index, genomic heterozygosity, endosymbiotic genetic discordance, as well as the hybrid index and heterozygosity of endosymbiotic genes (see Genomic Hybrid Index and Endosymbiotic Genetic Discordance). In addition, we recorded the blood total energy capacity and life history morphometrics.

Bioenergetic Endosymbiotic Synthesis Structural Equation Model (BES-SEM)

To predict the effect of climate change and hybridization on blood cell energetics and life history morphometrics, we built a structural equation model (SEM) for a bioenergetic

endosymbiotic synthesis (BES). The BES-SEM has a measurement model with three latent variables, and a structural model with three layers: (1) a molecular mediator layer, (2) an energetic mediator layer, and (3) the life history outcome layer. The three latent variables (η_1, η_2, η_3) are respectively indicated with a set of measurement variables. Specifically, η_1 reflects climate changes, and is presented by scaled climate scores for temperature (p_T), precipitation (p_p), and vapor pressure (p_v); η_2 represents genetic ancestry, indicated by the genomic hybrid index and the hybrid index of endosymbiotic genes; η_3 represents genetic discordance, synthesizing genomic heterozygosity, heterozygosity of endosymbiotic genes, and genetic discordance within endosymbiotic genes. The latent variables are then linked to the molecular mediator layer with (1) PC1 of endosymbiotic gene expression level; (2) endosymbiotic synergy measured by the global efficiency of ECNs (see ECN section). The molecular mediator layer then predicts the energetic mediator layer with total energy capacity (see Blood Cell Bioenergetics section). The mediator layer further predicts the outcome layer with the PC1 and PC2 of life history morphometrics. Across layers, the indirect effects from each latent variable to each mediator and outcome variable are incorporated. The BES-SEM is constructed with *lavaan* package[112] in R. The full hierarchical SEM is estimated with maximum likelihood. The 95% confidence intervals for each indirect effect are computed with bias-corrected and accelerated bootstrap resampling with 1,000 replications.

Data Availability Statement

All the raw data involved in this article have been submitted to SRA.

Competing Interest

We declare no competing interest.

Table 1 Significant association between climate variables and endosymbiotic gene expression.

	Effect Size ($\eta 2$)	95% CI	*p_var*	R^2	*p_overall*
Prec_1970 to 2000	0.70	[0.55, 1.00]	10^{-9}	0.864	10^{-13}
Prec_2024	0.74	[0.61, 1.00]	10^{-10}		
Species	0.52	[0.30, 1.00]	10^{-5}		
Temp_1970 to 2000	0.61	[0.42, 1.00]	10^{-7}	0.871	10^{-13}
Temp_2024	0.67	[0.51, 1.00]	10^{-8}		
Species	0.76	[0.63, 1.00]	10^{-10}		
VP_1970 to 2000	0.88	[0.81, 1.00]	10^{-15}	0.887	10^{-14}
VP_2024	0.21	[0.04, 1.00]	0.006		
Species	0.21	[0.02, 1.00]	0.021		

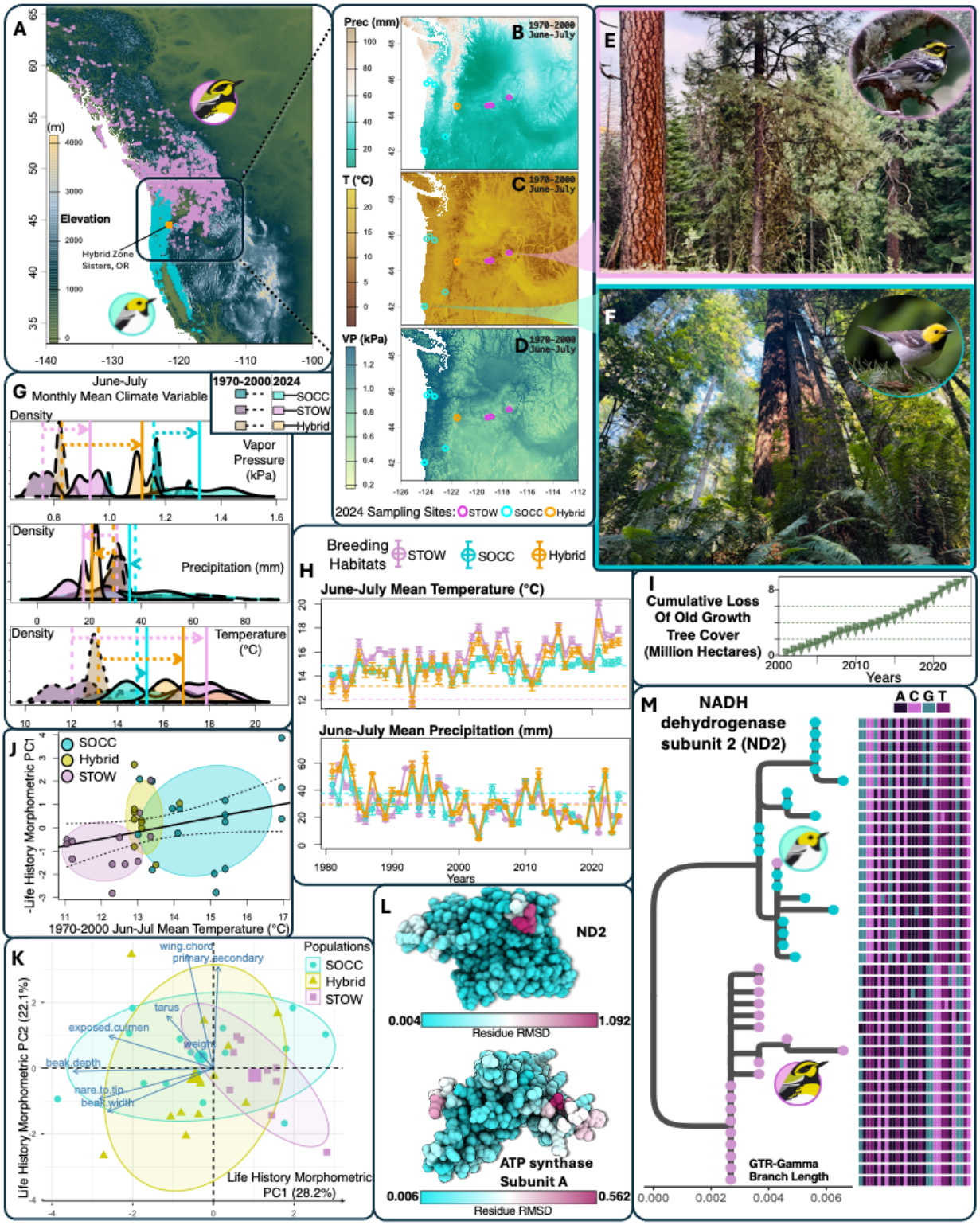


Fig. 1 Climatic gradient of the wood warbler breeding habitats and signatures of local climatic adaptation. (A) The breeding range of SOCC and STOW with elevation presented in meters. **(B-D)** Sampling locations of this study are labeled over the historical climatic baseline (June-July, 1970-2000) for monthly precipitation (Prec),

mean temperature (T) and vapor pressure (VP). **(E-F)** Breeding habitat photos of SOCC (E) and STOW (F) by Silu Wang. SOCC and STOW portraits by Frode Jacobsen and Silu Wang, respectively. **(G)** Current breeding habitats are significantly warmer and dryer than they were in 1970-2000. Arrows indicate the direction of changes in precipitation, temperature, and vapor pressure. **(H)** Yearly changes of the average June-July temperature (top) and precipitation (bottom) between 1980 and 2023 at the sampling sites of this study. **(I)** Loss of old-growth tree coverage between 2000 and 2023 in forests of WA, OR, ID, and CA, USA. **(J)** PC1 of life history morphometrics is significantly correlated with the historical breeding season temperature. Dots represent individual warbler samples. **(K)** PCA of life history morphometrics of breeding adults. PC1 reflects beak shape and PC2 represents wing size. **(L)** Sequence-based modeling predicts divergent 3D protein structures of NADH dehydrogenase subunit 2 (ND2) and ATP synthase subunit A between SOCC and STOW. The magenta components are residues with high dissimilarity between SOCC and STOW in per-residue root mean square deviation (RMSD). **(M)** SOCC and STOW harbor distinct mitochondrial ancestries within the ND2 gene that were previously shown to covary with climatic conditions in ancient hybrid populations[5]. Maximum likelihood gene tree of ND2 with nucleotide alignment of top 30 most divergent substitutions suggests near-reciprocal-monophyly.

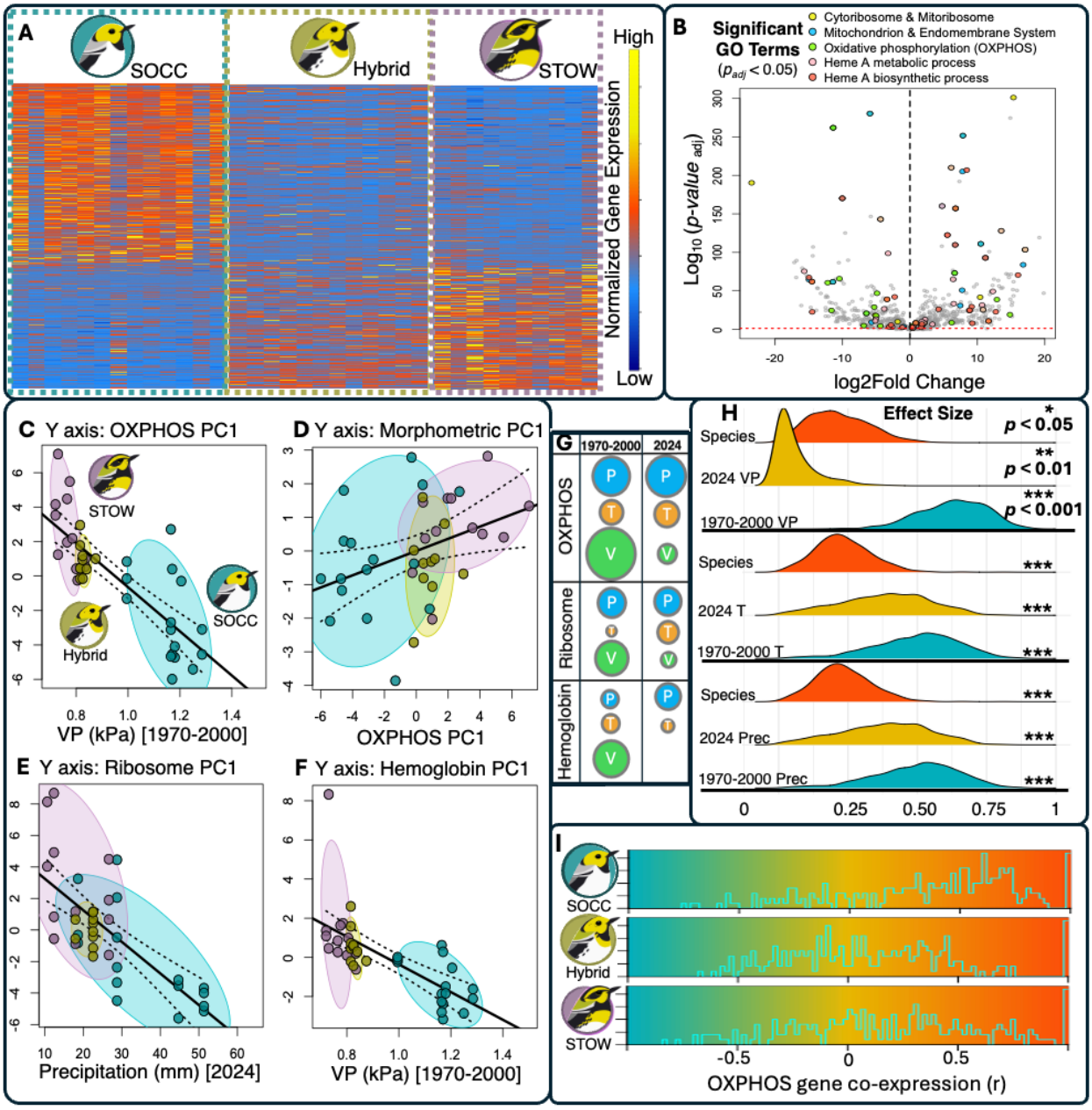

A
SOCC
Hybrid
STOW
High
Low
Normalized Gene Expression
B
Significant GO Terms (p_{adj} < 0.05)
Cytoribosome & Mitoribosome
Mitochondrion & Endomembrane System
Oxidative phosphorylation (OXPHOS)
Heme A metabolic process
Heme A biosynthetic process
Log10 (p-value adj)
log2Fold Change
C Y axis: OXPHOS PC1
VP (kPa) [1970-2000]
D Y axis: Morphometric PC1
OXPHOS PC1
E Y axis: Ribosome PC1
Precipitation (mm) [2024]
F Y axis: Hemoglobin PC1
VP (kPa) [1970-2000]
G
1970-2000
2024
OXPHOS
Ribosome
Hemoglobin
H
Effect Size
p < 0.05
p < 0.01
p < 0.001
Species
2024 VP
1970-2000 VP
2024 T
1970-2000 T
2024 Prec
1970-2000 Prec
I
OXPHOS gene co-expression (r)

Fig. 2 Endosymbiotic transcriptional divergence and climate adaptation. (A) Genes of differential expression (N = 2,037) between SOCC (turquoise box) and STOW (magenta box) display intermediate expression in hybrids (yellow box). **(B)** The differential genes are most enriched for factors involved in the endosymbotic bioenegetic cooperation among mitochondria, ribosomes, and nucleus. **(C-D)** Transcription PC1 of differential genes involved in OXPHOS is significantly ($p < 0.05$) associated with the historical vapor pressure (**C**) and the PC1 of life history morphometrics (**D**). **(E)** Transcription PC1 of differentially expressed mitoribosomal and cytoribosomal genes are negatively assocaited ($p < 0.05$) with the precipitation in 2024. **(F)** Transcription PC1 of differential genes involved in Hemoglobin Synthesis is negatively associated with VP in 1970-2000, but not with VP in 2024 (Table S3). **(G)** Relative effect sizes of the associations between climate variables (P, precipitation; T, temperature; V, vapor pressure) and the transcription PC1 of differential genes involved in (1) OXPHOS, (2) Ribosomal, and (3) Hemoglobin Synthesis. Both historical and present climate variables are incorperated in the same model that predicts each transcription PC1. Circles represent statistically significant effects of the corresponding climate variables. Circle size is proportional to the effect size. All the association analyses in **C**-**G** have controlled for species effect (Table 1, S1-S4). **(H)** Bootstrap distributions of effect sizes of three regression models that predict the PC1 of the differential genes by climate and species variables. The climate predictors are vapor pressure (VP), temperature (T), and precipitation (Prec). Both historical and present climate variables significantly explain the transcription PC1 of differential genes after controlling for species effect (Table 1). Historical climatic variables (blue) have larger effect sizes than the 2024 counterparts (yellow). **(C-H)** Transcription PC1s are positively associated with mean transcription levels of each individual (Fig. S1). **(I)** Density distribution of co-expression coefficients among OXPHOS genes. High frequencies of positive co-expression are observed in SOCC but not STOW or hybrids.

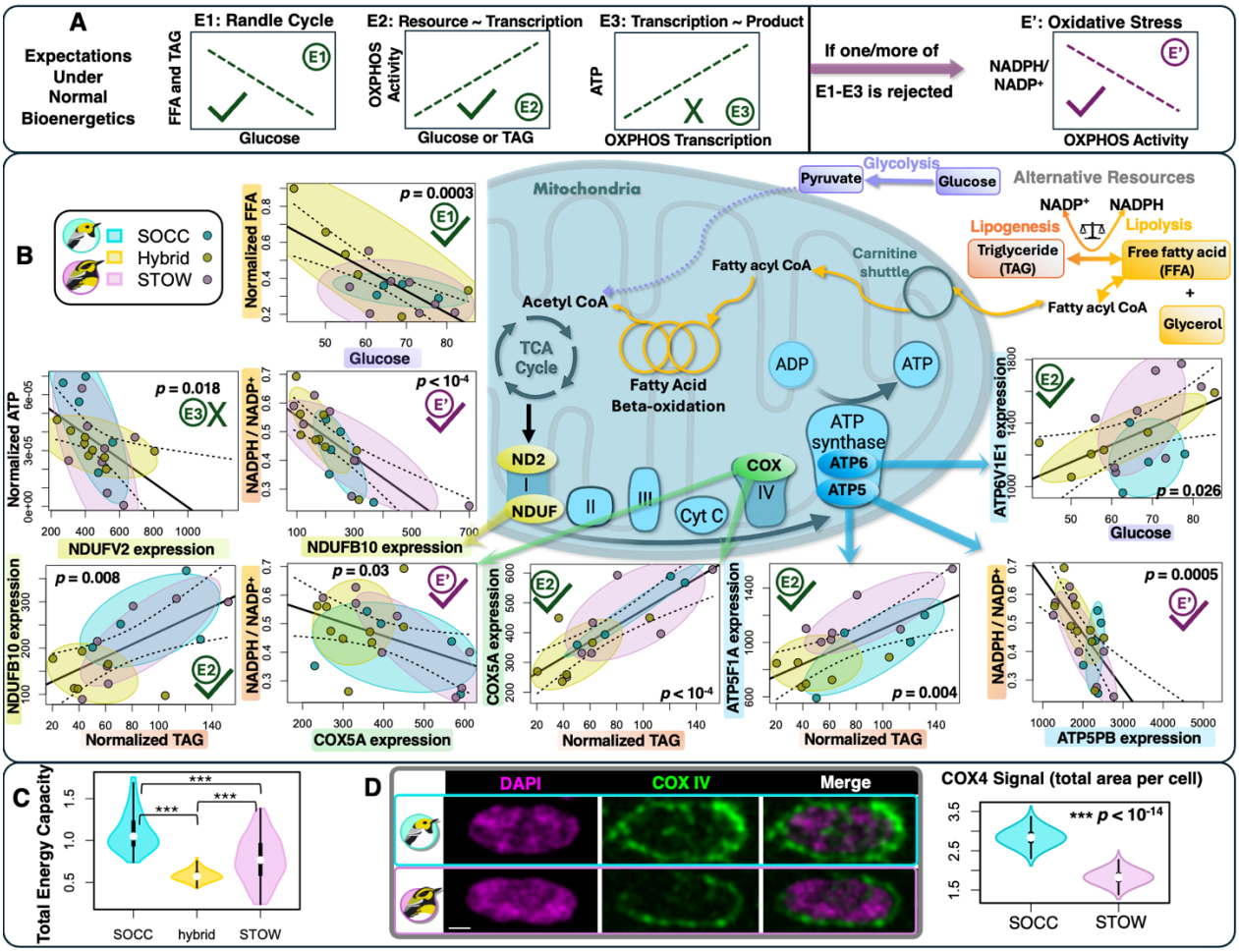

A
Expectations Under Normal Bioenergetics
E1: Randle Cycle
FFA and TAG
Glucose
E2: Resource ~ Transcription
OXPHOS Activity
Glucose or TAG
E3: Transcription ~ Product
ATP
OXPHOS Transcription
If one/more of E1-E3 is rejected
E': Oxidative Stress
NADPH/ NADP+
OXPHOS Activity
B
SOCC
Hybrid
STOW
Normalized FFA
p = 0.0003
Glucose
Mitochondria
Pyruvate
Glycolysis
Glucose
Alternative Resources
NADP+
NADPH
Lipogenesis
Lipolysis
Triglyceride (TAG)
Free fatty acid (FFA)
Glycerol
Fatty acyl CoA
Carnitine shuttle
Acetyl CoA
TCA Cycle
Fatty Acid Beta-oxidation
ADP
ATP
ATP synthase
ATP6
ATP5
ND2
NDUF
II
III
Cyt C
COX
IV
Normalized ATP
p = 0.018
NDUFV2 expression
NADPH / NADP+
p < 10-4
NDUFB10 expression
ATP6V1E1 expression
p = 0.026
NDUFB10 expression
p = 0.008
Normalized TAG
p = 0.03
COX5A expression
COX5A expression
p < 10-4
Normalized TAG
ATP5F1A expression
p = 0.004
Normalized TAG
p = 0.0005
ATP5PB expression
C
Total Energy Capacity
SOCC
hybrid
STOW
D
DAPI
COX IV
Merge
COX4 Signal (total area per cell)
*** p < 10-14
SOCC
STOW

Fig. 3 Endosymbiotic bioenergetics of the warbler blood cells sampled in the 2024 breeding season. (A) Expected features of normal (E1-E3) or stressed (E') metabolism that are consistent with (checkmarks) or contradicted (crossed, E3) by metabolite quantification of blood cells in this study. **E1**, Randle Cycle, where alternative fuel sources negatively associate during healthy cell metabolism. **E2**, normal OXPHOS expression positively associates with energy source. **E3**, OXPHOS expression normally positively predicts the ATP level. **E'**, a negative correlation between OXPHOS expression and NADPH/$NADP^+$ ratio indicates oxidative stress. **(B)** Quantification of metabolites and transcriptomics supports E1 and E2 but contradicts E3, reflecting metabolism under a potentially stressed state that is further indicated by E'. **E1** was supported: a negative association of glucose and FFA (top left, $p < 0.05$) supports the Randle Cycle, featuring the competing glycolysis (purple) versus lipolysis (orange) as alternative energy sources. **E2** was supported: expression of various OXPHOS genes collectively and positively correlates with energy sources, glucose and TAG, fulfilling energy demand via enhanced metabolism (Table S4-S5). **E3** was not supported: a potential disorder in OXPHOS function in that ATP abundance is not positively correlated with OXPHOS gene expression (Table S6). Signatures of **E'**: an indication of oxidative stress is suggested by the negative correlation between NADPH/$NADP^+$ ratio and OXPHOS gene expression ($p < 0.05$), reflecting the depleted NADPH reserve for antioxidant defense (Table S7). **(C)** ATP and energy source substrate ATP conversion indicates that SOCC (bootstrap 95% CI: 0.81-1.69) has significantly higher total energy capacity than STOW (bootstrap 95% CI: 0.28-1.29), which surpasses hybrids (bootstrap 95% CI: 0.47-0.72). **(D)** Confocal imaging visualizes the mitochondrial inner membrane (anti-COX IV) and nuclei (DAPI) of blood cells and elucidates a significantly larger mitochondrial inner membrane area per blood cell in SOCC than STOW ($p < 0.05$). Scale bar: 1 μm. Three biological replicates per species.

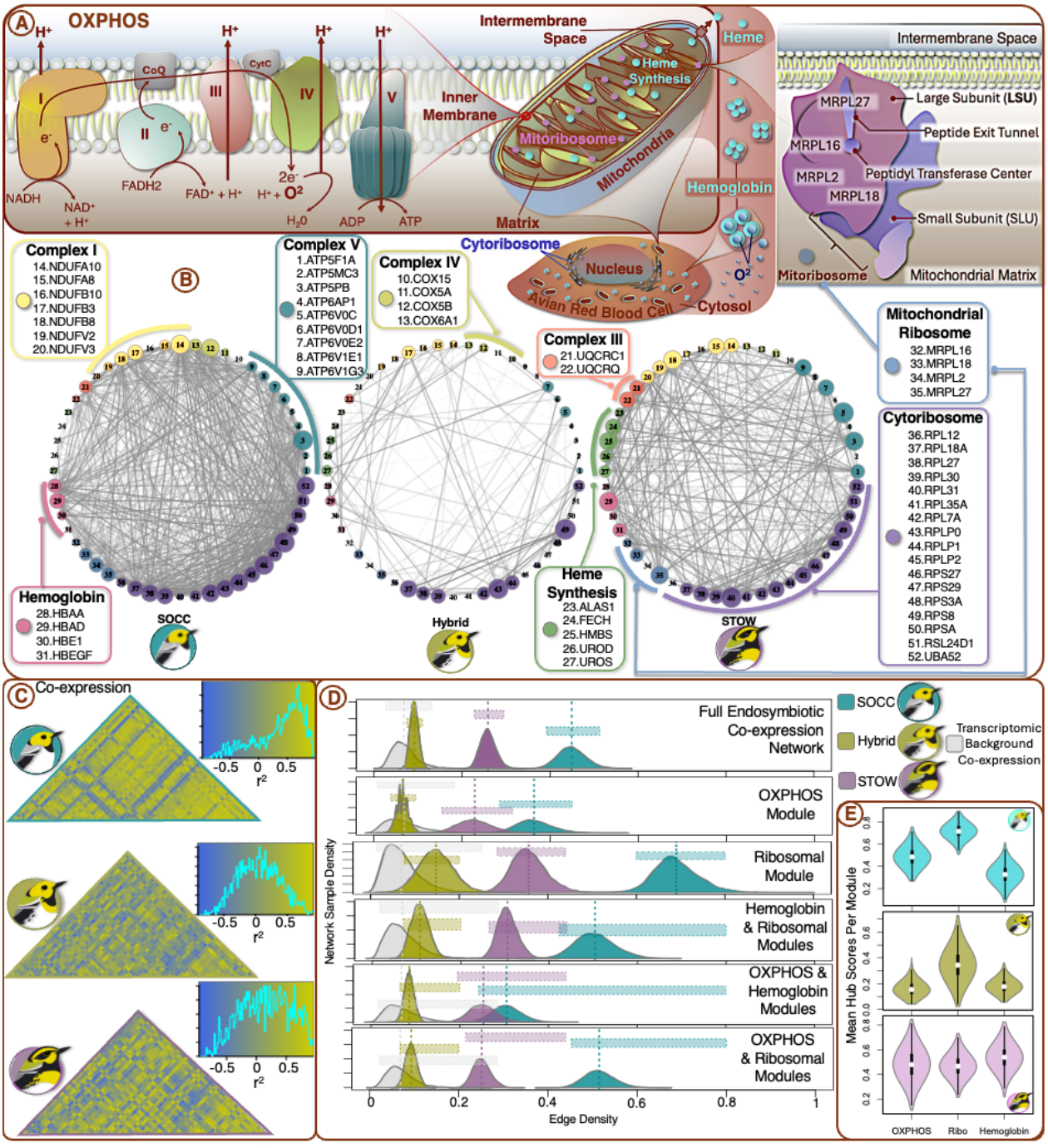
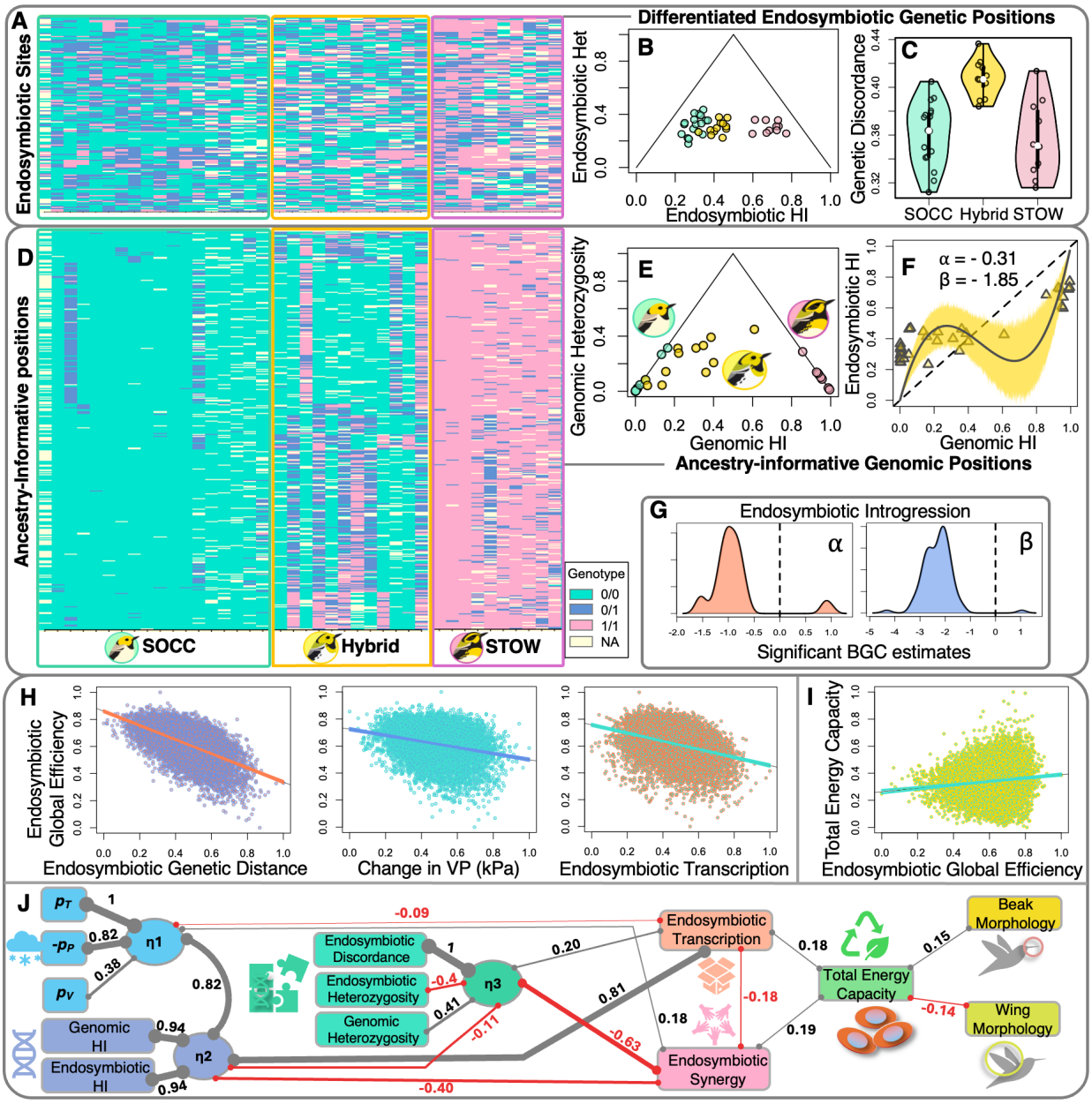

A
OXPHOS
Intermembrane Space
Inner Membrane
Matrix
Heme
Heme Synthesis
Mitoribosome
Mitochondria
Hemoglobin
Cytoribosome
Nucleus
Avian Red Blood Cell
Cytosol
MRPL27
Large Subunit (LSU)
Peptide Exit Tunnel
MRPL16
MRPL2
Peptidyl Transferase Center
MRPL18
Small Subunit (SLU)
Mitochondrial Matrix
B
Complex I
14.NDUFA10
15.NDUFA8
16.NDUFB10
17.NDUFB3
18.NDUFB8
19.NDUFV2
20.NDUFV3
Complex V
1.ATP5F1A
2.ATP5MC3
3.ATP5PB
4.ATP6AP1
5.ATP6V0C
6.ATP6V0D1
7.ATP6V0E2
8.ATP6V1E1
9.ATP6V1G3
Complex IV
10.COX15
11.COX5A
12.COX5B
13.COX6A1
Complex III
21.UQCRC1
22.UQCRQ
Mitochondrial Ribosome
32.MRPL16
33.MRPL18
34.MRPL2
35.MRPL27
Cytoribosome
36.RPL12
37.RPL18A
38.RPL27
39.RPL30
40.RPL31
41.RPL35A
42.RPL7A
43.RPLP0
44.RPLP1
45.RPLP2
46.RPS27
47.RPS29
48.RPS3A
49.RPS8
50.RPSA
51.RSL24D1
52.UBA52
Heme Synthesis
23.ALAS1
24.FECH
25.HMBS
26.UROD
27.UROS
Hemoglobin
28.HBAA
29.HBAD
30.HBE1
31.HBEGF
SOCC
Hybrid
STOW
C
Co-expression
r²
D
Full Endosymbiotic Co-expression Network
OXPHOS Module
Ribosomal Module
Hemoglobin & Ribosomal Modules
OXPHOS & Hemoglobin Modules
OXPHOS & Ribosomal Modules
Network Sample Density
Edge Density
SOCC
Hybrid
STOW
Transcriptomic Background Co-expression
E
Mean Hub Scores Per Module
OXPHOS
Ribo
Hemoglobin

Fig. 4 Endosymbiotic Co-expression Networks, ECN. (A) Demonstration of endosymbiotic functions in avian red blood cells, featuring cytoribosome, mitoribosome, hemoglobin synthesis, as well as OXPHOS proteins involved in electron transport chain (Complex I-IV) and ATP synthase (Complex V). The core subunits of OXPHOS proteins (complexes I-V) are translated in mitoribosomes, and utilize oxygen delivered by hemoglobin to generate ATP. These key components are highly enriched among genes of differential expression between SOCC and STOW (Fig. 2 B). **(B)** Endosymbiotic Co-expression Networks of SOCC, hybrids, and STOW. Each node represents an endosymbiotic gene, which shares the same color to its encoded functional protein in panel A. Each edge (line) connecting two genes represents a significant co-expression relationship, with the line darkness in proportion to its weight (absolute value of pairwise correlation coeffcient r^2). The node size represents its strength, which is the weight sum of all its edge connections. Each endosymbiotic co-expression network consists of three main functional modules (1) OXPHOS-encoded components of Complexes I, III, IV, V in yellow, orange, green, and blue respectively; (2) hemoglobin genes involved in heme-synthesis (dark green) and hemoglobin subunits (pink); and (3) ribosome components that include mitoribosomal (dark blue) and cytoribosomal (purple) factors. **(C)** Heatmaps showing pairwise correlation coeffcients (r^2) among the transcription levels of endosymbiotic genes in SOCC, hybrids and STOW. SOCC shows higher frequencies of strong positive co-expression than STOW and hybrids. **(D)** The edge density within each network or module class reflects co-expression strength as a proxy of the synergy among endosymbiotic genes. The SOCC network (turquoise) exhibits much higher endosymbiotic synergy than STOW (magenta) and hybrids (gold) in the full network (top), within the OXPHOS module, within the ribosomal module, and among modules. The 95% CI of each distribution is represented by the horizontal rectangles above the corresponding density curve. **(E)** The bootstrap mean of hub centrality across OXPHOS, Ribosomal, and Hemoglobin Modules.

923


A
Endosymbiotic Sites
Differentiated Endosymbiotic Genetic Positions
B
Endosymbiotic Het
Endosymbiotic HI
C
Genetic Discordance
SOCC Hybrid STOW
D
Ancestry-Informative positions
SOCC
Hybrid
STOW
Genotype
0/0
0/1
1/1
NA
E
Genomic Heterozygosity
Genomic HI
F
α = - 0.31
β = - 1.85
Endosymbiotic HI
Genomic HI
Ancestry-informative Genomic Positions
G
Endosymbiotic Introgression
α
β
Significant BGC estimates
H
Endosymbiotic Global Efficiency
Endosymbiotic Genetic Distance
Change in VP (kPa)
Endosymbiotic Transcription
I
Total Energy Capacity
Endosymbiotic Global Efficiency
J
pT
-pP
pV
η1
η2
η3
Genomic HI
Endosymbiotic HI
Endosymbiotic Discordance
Endosymbiotic Heterozygosity
Genomic Heterozygosity
Endosymbiotic Transcription
Endosymbiotic Synergy
Total Energy Capacity
Beak Morphology
Wing Morphology
1
0.82
0.38
0.82
0.94
0.94
-0.09
1
-0.4
0.41
-0.11
0.20
0.81
-0.63
-0.40
0.18
-0.18
0.19
0.18
0.15
-0.14

924
925

Fig. 5 Endosymbiotic synergistic response to climate change: endosymbiotic introgression across the wood warbler species boundary. (A) Genotypes of divergent genetic positions within the endosymbiotic genes. **(B)** Triangle plot characterizing genetic hybrid index (HI) and heterozygosity of reflects admixture patterns within endosymbiotic genes. Each dot represents one warbler. **(C)** Hybrids display significantly more genetic discordance than the parental species ($p < 0.05$). **(D)** Genotypes of ancestry-informative positions across the genome in SOCC, STOW, and hybrids. Each column represents one warbler. **(E)** Triangle plot showing the genomic HI and heterozygosity across SOCC (turquoise), STOW (magenta), and hybrids (gold). **(F)** Bayesian Genomic Cline (BGC) analysis characterizing the deviation of ancestry within endosymbiotic genes relative to the genomic background in hybrids and parental species. BGC reveals excessive SOCC-biased introgression in endosymbiotic genes. **(G)** Distribution of the significant ($p < 0.05$) BGC estimates of introgression direction (α) and rate (ß) across endosymbiotic genes are predominantly negative, consistent with the excessive SOCC-biased introgression. **(H)** The simulated networks generated with random samples from the panmictic population (with SOCC, STOW, and hybrids) reveal that endosymbiotic molecular synergy represented by the global efficiency of the endosymbiotic co-expression network is significantly ($p < 0.05$) and negatively predicted by the genetic discordance of endosymbiotic genes, the changes in vapor pressure between 1970-2000 and 2024, and the transcription level of endosymbiotic genes. **(I)** Endosymbiotic synergy in the networks sampled from the simulated panmictic population positively predicts total energy capacity (ATP and energy source substrate ATP conversion) of the blood cells. **(J)** Bioenergetic Endosymbiotic Synthesis Structural Equation Model (BES-SEM). To predict organismal responses to climate change, BES-SEM integrates the effects of climate change, transcriptomics, genomic composition by hybridization, blood bioenergetics, and life history morphometrics. The positive versus negative relationships is represented by grey and red lines, respectively, with the effect sizes (above the paths) are standardized path coefficients of significant paths. Line thickness proportional to effect size.

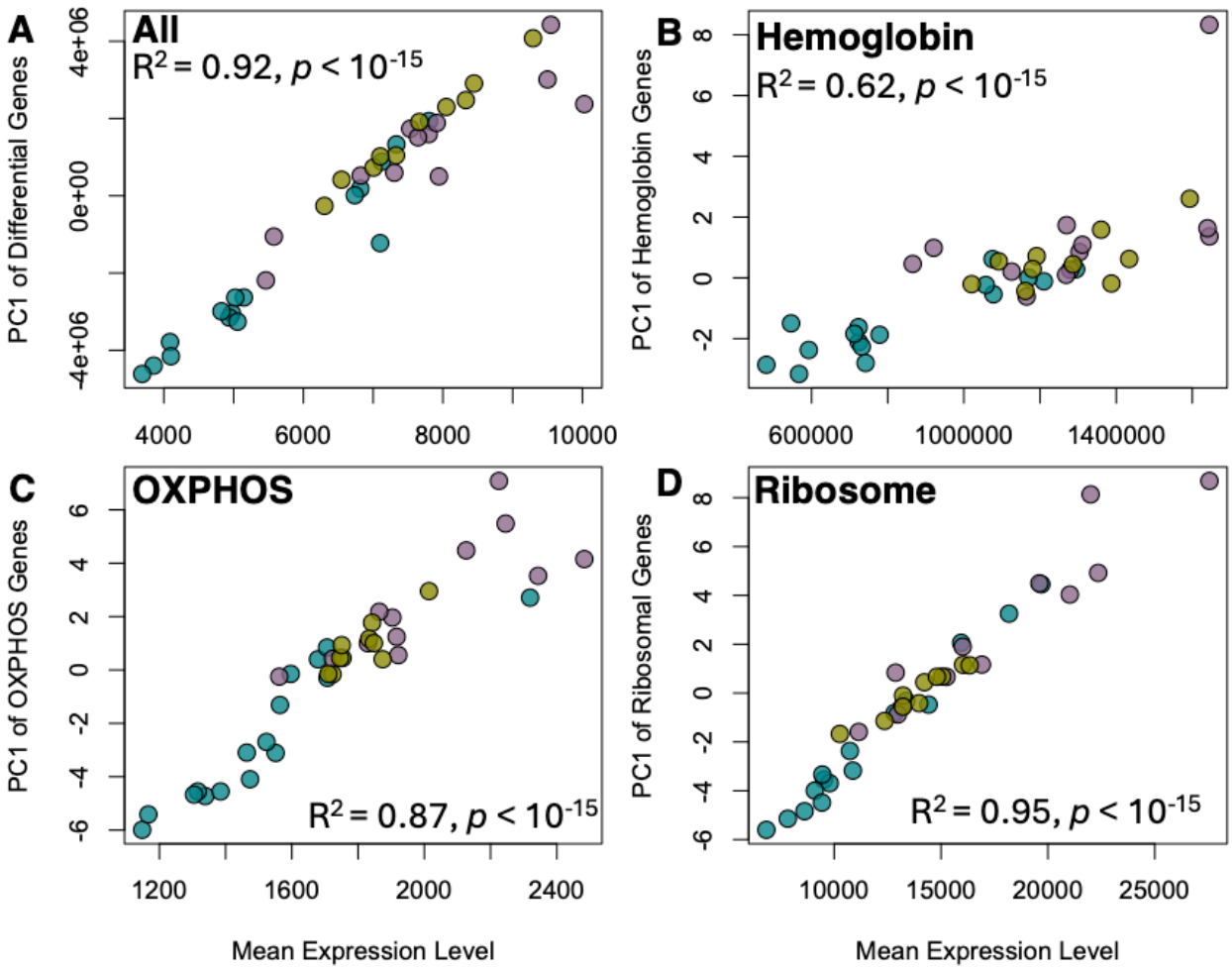


Fig.S1 The positive associations between transcription PC1 and gene expression levels of **(A)** all 2,037 differential genes, **(B)** Hemoglobin synthesis genes, **(C)** OXPHOS genes, and **(D)** Ribosomal genes. Turquoise, SOCC; yellow, hybrids; magenta, STOW. Each dot represents one warbler.

References

1. Sagan, L. On the origin of mitosing cells. *J. Theor. Biol.* **14**, 225-IN6 (1967).
2. Berry, S. Endosymbiosis and the design of eukaryotic electron transport. *Biochim. Biophys. Acta BBA - Bioenerg.* **1606**, 57–72 (2003).
3. Sloan, D. B., Havird, J. C. & Sharbrough, J. The on-again, off-again relationship between mitochondrial genomes and species boundaries. *Mol. Ecol.* **26**, 2212–2236 (2017).
4. Hill, G. E. The mitonuclear compatibility species concept. *The Auk* **134**, 393–409 (2017).
5. Wang, S. *et al.* Signatures of mitonuclear coevolution in a warbler species complex. *Nat. Commun.* **12**, 4279 (2021).
6. Moran, B. M. *et al.* A lethal mitonuclear incompatibility in complex I of natural hybrids. *Nature* **626**, 119–127 (2024).
7. Wang, S., Mank, J. E., Ortiz-Barrientos, D. & Rieseberg, L. H. Genome architecture and speciation in plants and animals. *Mol. Ecol.* **34**, e70004 (2025).
8. Burton, R. S. The role of mitonuclear incompatibilities in allopatric speciation. *Cell. Mol. Life Sci.* **79**, 103 (2022).
9. Quirós, P. M, Mottis, A. & Auwerx, J. Mitonuclear communication in homeostasis and stress. *Nat. Rev. Mol. Cell Biol.* **17**, 213–226 (2016).
10. Sokolova, I. M. Ectotherm mitochondrial economy and responses to global warming. *Acta Physiol.* **237**, e13950 (2023).
11. Keefe *et al.* Mitochondrial adaptations from heat acclimation: A narrative review. *J. Therm. Biol.* **133**, 104283 (2025).

12. Grover-Thomas, F., Van Dorp, L., Balloux, F., Andrés, A. M. & Camus, M. F. Climate-associated natural selection in the human mitochondrial genome. *Mol. Biol. Evol.* **43**, msag044 (2026).

13. Mishmar, D. *et al.* Natural selection shaped regional mtDNA variation in humans. *Proc. Natl. Acad. Sci.* **100**, 171–176 (2003).

14. Camus, M. F., Wolff, J. N., Sgrò, C. M. & Dowling, D. K. Experimental Support That Natural Selection Has Shaped the Latitudinal Distribution of Mitochondrial Haplotypes in Australian Drosophila melanogaster. *Mol. Biol. Evol.* **34**, 2600–2612 (2017).

15. Raval PK, MacLeod AI, & Gould SB. A molecular atlas of plastid and mitochondrial proteins reveals organellar remodeling during plant evolutionary transitions from algae to angiosperms. *PLOS Biol.* **22**, e3002608 (2024).

16. Clark, A. G. NATURAL SELECTION WITH NUCLEAR AND CYTOPLASMIC TRANSMISSION. I. A DETERMINISTIC MODEL. *Genetics* **107**, 679–701 (1984).

17. Rand, D. M., Haney, R. A. & Fry, A. J. Cytonuclear coevolution: the genomics of cooperation. *Trends Ecol. Evol.* **19**, 645–653 (2004).

18. Hill, G. E. *Mitonuclear Ecology*. (Oxford University Press, 2019). doi:10.1093/oso/9780198818250.001.0001.

19. Wolff, J. N., Ladoukakis, E. D., Enríquez, J. A. & Dowling, D. K. Mitonuclear interactions: evolutionary consequences over multiple biological scales. *Philos. Trans. R. Soc. B Biol. Sci.* **369**, 20130443 (2014).

20. Havird, J. C. *et al.* Selfish Mitonuclear Conflict. *Curr. Biol.* **29**, R496–R511 (2019).

21. Archibald, J. M. Endosymbiosis and Eukaryotic Cell Evolution. *Curr. Biol.* **25**, R911–R921 (2015).

22. Isaac, R. S., McShane, E. & Churchman, L. S. The Multiple Levels of Mitonuclear Coregulation. *Annu. Rev. Genet.* **52**, 511–533 (2018).

23. Kim, K. H. & Lee, C. B. Socialized mitochondria: mitonuclear crosstalk in stress. *Exp. Mol. Med.* **56**, 1033–1042 (2024).

24. Antolínez-Fernández, Á., Esteban-Ramos, P., Fernández-Moreno, M. Á. & Clemente, P. Molecular pathways in mitochondrial disorders due to a defective mitochondrial protein synthesis. *Front. Cell Dev. Biol.* **12**, 1410245 (2024).

25. Popov LD. Mitochondrial biogenesis: an update. **24**, 4892–4899 (2020).

26. Medeiros, D. M. Assessing mitochondria biogenesis. *Methods* **46**, 288–294 (2008).

27. Mai, N., Chrzanowska-Lightowlers, Z. M. A. & Lightowlers, R. N. The process of mammalian mitochondrial protein synthesis. *Cell Tissue Res* **367**, 5–20 (2017).

28. McShane, E. *et al.* A kinetic dichotomy between mitochondrial and nuclear gene expression processes. *Mol. Cell* **84**, 1541-1555.e11 (2024).

29. Liu CT, B. G. Mild heat stress induces mitochondrial biogenesis in C2C12 myotubes. *J Appl Physiol* **112**, 354–361 (2012).

30. Sonenberg, N., Hinnebusch, & A. G. Regulation of translation initiation in eukaryotes. *Cell* **136**, 731–745 (2009).

31. Rahaman, S. *et al.* Heat shock induces silent ribosomes and reorganizes mRNA turnover. *Cell Rep.* **44**, 116447 (2025).

32. Salgado RM *et al.* Mitochondrial efficiency and exercise economy following heat stress: a potential role of uncoupling protein. *Physiol. Rep.* **5**, e13054 (2017).

33. Patton MG *et al.* Heat acclimation increases mitochondrial respiration capacity of C2C12 myotubes and protects against LPS-mediated energy deficit. *Cell Stress Chaperones* **23**, 871–883 (2018).

34. Cao, X. *et al.* Effects of N-acetyl-L-cysteine on chronic heat stress-induced oxidative stress and inflammation in the ovaries of growing pullets. *Poult. Sci.* **102**, 102274 (2023).

35. Larsen S *et al.* Biomarkers of mitochondrial content in skeletal muscle of healthy young human subjects. *J. Physiol.* **590**, 3349–3360 (2012).

36. Gerashchenko, M.V. Alexei V. Lobanov, & Vadim N. Gladyshev. Genome-wide ribosome profiling reveals complex translational regulation in response to oxidative stress. *Proc. Natl. Acad. Sci. U. S. A.* **109**, 17394–17399 (2012).

37. Tamura Y *et al.* Postexercise whole body heat stress additively enhances endurance training-induced mitochondrial adaptations in mouse skeletal muscle. *Am. J. Physiol.-Regul. Integr. Comp. Physiol.* **307**, R931–R943 (2014).

38. Rohwer, S. & Wood, C. Three Hybrid Zones between Hermit and Townsend's Warblers in Washington and Oregon. *The Auk* **115**, 284–310 (1998).

39. Wang, S., Rohwer, S., Delmore, K. & Irwin, D. E. Cross-decades stability of an avian hybrid zone. *J. Evol. Biol.* **32**, 1242–1251 (2019).

40. Wang, S. *et al.* Selection on a small genomic region underpins differentiation in multiple color traits between two warbler species. *Evol. Lett.* **4**, 502–515 (2020).

41. de Zwaan, D. R., Mackenzie, J., Mikkelsen, E., Wood, C. & Wang, S. Pleiotropic opposing dominance within a color gene block contributes to a nascent species boundary via its influence on hybrid male territorial behavior. *PNAS Nexus* **1**, pgac074 (2022).

42. Krosby, M. & Rohwer, S. A 2000 km genetic wake yields evidence for northern glacial refugia and hybrid zone movement in a pair of songbirds. *Proc. R. Soc. B Biol. Sci.* **276**, 615–621 (2009).

43. Pennycuick, C. J. Mechanics of flight. In Avian Biology (ed. D. S. Farner), pp.1-75. New York: Academic Press. in (1975).

44. Swartz, S. Kenneth S. Breuer, & David J. Willis. Aeromechanics in aeroecology: flight biology in the aerosphere, Integrative and Comparative Biology. *48:85–98* https://doi.org/10.1093/icb/icn064 (2008) doi:10.1093/icb/icn064.

45. Muñoz-Garcia *et al.* Metabolic rate, evaporative water loss and thermoregulatory state in four species of bats in the Negev desert. *Comp. Biochem. Physiol. A. Mol. Integr. Physiol.* **191**, 156–165 (2016).

46. Wiens, J. J., & Graham, C. H. 2005. Niche conservatism: Integrating evolution, ecology, and conservation biology. Annual Review of Ecology, Evolution, and Systematics. 36: 519–539. https://doi.org/10.1146/annurev.ecolsys.36.102803.095431 doi:10.1146/annurev.ecolsys.36.102803.095431.

47. Tamura Y, Matsunaga Y, Masuda H, Takahashi Y, Takahashi Y, Terada S, et al. 2014. Postexercise whole body heat stress additively enhances endurance training-induced mitochondrial adaptations in mouse skeletal muscle. Am. The Journal of Physiology.

Regul. Integr. Comp. Physiol 307: R931–R943.
https://doi.org/10.1152/ajpregu.00426.2013 doi:10.1152/ajpregu.00426.2013.
48. Randle, P.J. P. B. Garland, C. N. Hales, & E. A. Newsholme. The glucose fatty-acid cycle: Its role in insulin sensitivity and the metabolic disturbances of diabetes mellitus. *The Lancet* **281**, 785–789 (1963).
49. Bhatti, J. S., Bhatti, G. K. & Reddy, P. H. Mitochondrial dysfunction and oxidative stress in metabolic disorders — A step towards mitochondria based therapeutic strategies. *Biochim. Biophys. Acta BBA - Mol. Basis Dis.* **1863**, 1066–1077 (2017).
50. Devin, A. & Rigoulet, M. Mechanisms of mitochondrial response to variations in energy demand in eukaryotic cells. *Am. J. Physiol.-Cell Physiol.* **292**, C52–C58 (2007).
51. Rolfe, D. F. & Brown, G. C. Cellular energy utilization and molecular origin of standard metabolic rate in mammals. *Physiol. Rev.* **77**, 731–758 (1997).
52. Rohas, L. M. *et al.* A fundamental system of cellular energy homeostasis regulated by PGC-1α. *Proc. Natl. Acad. Sci.* **104**, 7933–7938 (2007).
53. Jeon, S. M., Chandel, N. S. & Hay, N. AMPK regulates NADPH homeostasis to promote tumour cell survival during energy stress. *Nature* **485**, 661–665 (2012).
54. Lewis *et al.* Tracing compartmentalized NADPH metabolism in the cytosol and mitochondria of mammalian cells. *Mol. Cell* **55**, 253–263 (2014).
55. Moon, S. J. *et al.* Oxidative pentose phosphate pathway and glucose anaplerosis support maintenance of mitochondrial NADPH pool under mitochondrial oxidative stress. *Bioeng. Transl. Med.* **5**, e10184 (2020).

56. Schafer, Z. T. *et al.* Antioxidant and oncogene rescue of metabolic defects caused by loss of matrix attachment. *Nature* **461**, 109–113 (2009).

57. Larsen S *et al.* Biomarkers of mitochondrial content in skeletal muscle of healthy young human subjects. *J. Physiol.* https://doi.org/10.1113/jphysiol.2011.228296 (2012) doi:10.1113/jphysiol.2011.228296.

58. Salgado RM *et al.* Mitochondrial efficiency and exercise economy following heat stress: a potential role of uncoupling protein. *Physiol. Rep.* https://doi.org/10.14814/phy2.13054 (2017) doi:10.14814/phy2.13054.

59. Napolitano, G., Fasciolo, G. & Venditti, P. Mitochondrial Management of Reactive Oxygen Species. *Antioxidants* **10**, 1824 (2021).

60. Sonenberg, N., Hinnebusch, & A. G. Regulation of translation initiation in eukaryotes. *Cell* https://doi.org/10.1016/j.cell.2009.01.042 (2009) doi:10.1016/j.cell.2009.01.042.

61. Quirós, P. M, Mottis, A. & Auwerx, J. Mitonuclear communication in homeostasis and stress. *Nat. Rev. Mol. Cell Biol.* https://doi.org/10.1038/nrm.2016.23 (2016) doi:10.1038/nrm.2016.23.

62. Wakigawa, T. *et al.* Monitoring the complexity and dynamics of mitochondrial translation. *Mol. Cell* https://doi.org/10.1016/j.molcel.2025.10.022 (2025) doi:10.1016/j.molcel.2025.10.022.

63. Wang, S., Mank, J. E., Ortiz-Barrientos, D. & Rieseberg, L. H. Genome Architecture and Speciation in Plants and Animals. *Mol. Ecol.* e70004 (2025) doi:10.1111/mec.70004.

64. Khawaja, A., Cipullo, M., Krüger, A. & Rorbach, J. Insights into mitoribosomal biogenesis from recent structural studies. *Trends Biochem. Sci.* **48(7),** 629–641 (2023).

65. Storz JF. 2016. Hemoglobin-oxygen affinity in high-altitude vertebrates: is there evidence for an adaptive trend? Journal of Experimental Biology 219:3190-3203. https://doi.org/10.1242/jeb.132837 doi:10.1242/jeb.132837.

66. Felsenstein, J. Skepticism Towards Santa Rosalia, or Why are There so Few Kinds of Animals? *Evolution* **35**, 124 (1981).

67. Chapdelaine, V., Bettinazzi, S., Breton, S. & Angers, B. Effects of mitonuclear combination and thermal acclimation on the energetic phenotype. *J. Exp. Zool. Part Ecol. Integr. Physiol.* **333**, 264–270 (2020).

68. Havird, J. C. *et al.* Beyond the Powerhouse: Integrating Mitonuclear Evolution, Physiology, and Theory in Comparative Biology. *Integr. Comp. Biol.* **59**, 856–863 (2019).

69. Bettinazzi, S. *et al.* Assessing the role of mitonuclear interactions on mitochondrial function and organismal fitness in natural *Drosophila* populations. *Evol. Lett.* **8**, 916–926 (2024).

70. Butenko, A., Lukeš, J., Speijer, D. & Wideman, J. G. Mitochondrial genomes revisited: why do different lineages retain different genes? *BMC Biol.* **22**, 15 (2024).

71. Hill, G. E. Mitonuclear Compensatory Coevolution. *Trends Genet.* **36**, 403–414 (2020).

72. Timmis, J. N., Ayliffe, M. A., Huang, C. Y. & Martin, W. Endosymbiotic gene transfer: organelle genomes forge eukaryotic chromosomes. *Nat. Rev. Genet.* **5**, 123–135 (2004).

73. Couvillion, M. T., Soto, I. C., Shipkovenska, G. & Churchman, L. S. Synchronized mitochondrial and cytosolic translation programs. *Nature* **533**, 499–503 (2016).

74. Brischigliaro, M., Sierra-Magro, A., Ahn, A. & Barrientos, A. Mitochondrial ribosome biogenesis and redox sensing. *FEBS Open Bio* **14**, 1640–1655 (2024).

75. Mai, N., Chrzanowska-Lightowlers, Z. M. A. & Lightowlers, R. N. The process of mammalian mitochondrial protein synthesis. *Cell Tissue Res.* **367**, 5–20 (2017).

76. Allard, C. A. H. *et al.* A host organelle integrates stolen chloroplasts for animal photosynthesis. *Cell* **188**, 5266-5277.e13 (2025).

77. Peterson, A. T., Soberón, J. & Sánchez-Cordero, V. Conservatism of Ecological Niches in Evolutionary Time. *Science* **285**, 1265–1267 (1999).

78. Fick, S. E, & R. J. Hijmans. WorldClim 2: new 1-km spatial resolution climate surfaces for global land areas. *Int J Clim.* https://doi.org/10.1002/joc.5086 (2017) doi:10.1002/joc.5086.

79. Hansen *et al.* High-resolution global maps of 21st-century forest cover change. *Science* **342**, 850–853 (2013).

80. Wickham, H. httr: tools for working with URLs and HTTP. *R Package Version 147 HttpsCRANR-Proj.-Proj.* (2023).

81. Benson, D. A. *et al.* GenBank. *Nucleic Acids Res.* **41**, D36–D42 (2012).

82. Bodenhofer, U., Bonatesta, E., Horejš-Kainrath, C. & Hochreiter, S. msa: an R package for multiple sequence alignment. *Bioinformatics* **31**, 3997–3999 (2015).

83. Schliep K.P. phangorn: phylogenetic analysis in R. *Bioinformatics* **27**, 592–593 (2011).

84. Varadi, M. *et al.* AlphaFold Protein Structure Database: massively expanding the structural coverage of protein-sequence space with high-accuracy models. *Nucleic Acids Res.* https://doi.org/10.1093/nar/gkab1061 (2022) doi:10.1093/nar/gkab1061.

85. Pettersen *et al.* UCSF ChimeraX: structure visualization for researchers, educators, and developers. *Protein Sci* https://doi.org/10.1002/pro.3943 (2021) doi:10.1002/pro.3943.

86. De Coster *et al.* NanoPack: visualizing and processing long-read sequencing data. *Bioinformatics* **34**, 2666–2669 (2018).

87. Kolmogorov, M., J. Yuan, Y. Lin, & P. A. Pevzner. Assembly of long, error-prone reads using repeat graphs. *Nat. Biotechnol.* **37**, 540–546 (2019).

88. Oxford Nanopore Technologies. Medaka: sequence correction provided by ONT Research. *Available Httpsgithubcomnanoporetechmedakahttpsgithubcomnanoporetechmedaka* (2018).

89. Alonge, M. *et al.* Automated assembly scaffolding using RagTag elevates a new tomato system for high-throughput genome editing. *Genome Biol.* **23**, 258 (2022).

90. Flynn *et al.* RepeatModeler2 for automated genomic discovery of transposable element families. *Proc Natl Acad Sci USA* https://doi.org/10.1073/pnas.1921046117 (2020) doi:10.1073/pnas.1921046117.

91. Gabriel, L. *et al.* BRAKER3: fully automated genome annotation using RNA-seq and protein evidence with GeneMark-ETP, AUGUSTUS, and TSEBRA. *Genome Res.* https://doi.org/10.1101/gr.278090.123 (2024) doi:10.1101/gr.278090.123.

92. Camacho, C. *et al*. BLAST+: architecture and applications. *BMC Bioinformatics* **10**, 421 (2009).

93. Bolger, A. M., Lohse, M. & Usadel, B. Trimmomatic: a flexible trimmer for Illumina sequence data. *Bioinformatics* **30**, 2114–2120 (2014).

94. Li H & Durbin R. Fast and accurate short read alignment with Burrows-Wheeler transform. *Bioinformatics* **25**, 1754–1760 (2009).

95. Danecek, P. *et al*. The variant call format and VCFtools. *Bioinformatics* **27**, 2156–2158 (2011).

96. Chen D, McManus CE, Radmanesh B, Matzat LH, & Lei EP. Temporal inhibition of chromatin looping and enhancer accessibility during neuronal remodeling. *Nat. Commun*. **12**, 6366 (2021).

97. Chen, D., Keremane, S., Wang, S. & Lei, E. P. CTCF regulates global chromatin accessibility and transcription during rod photoreceptor development. *Proc. Natl. Acad. Sci.* **122**, e2416384122 (2025).

98. Martin, M. Cutadapt removes adapter sequences from high-throughput sequencing reads. *EMBnet.journal* **17**, 10–12 (2011).

99. Yang Liao, Gordon K. Smyth, & Wei Shi. featureCounts: an efficient general purpose program for assigning sequence reads to genomic features. *Bioinformatics* **30**, 923–930 (2014).

100. Love MI, Huber W, & Anders S. Moderated estimation of fold change and dispersion for RNA-seq data with DESeq2. *Genome Biol.* **15**, 550 (2014).

101. Raudvere, U. *et al.* g:Profiler: a web server for functional enrichment analysis and conversions of gene lists (2019 update). *Nucleic Acids Res.* **47**, W191–W198 (2019).

102. Baatz, M. & Wagner, G. P. Adaptive Inertia Caused by Hidden Pleiotropic Effects. *Theor. Popul. Biol.* **51**, 49–66 (1997).

103. Wasserman, S. & Faust, K. Social Network Analysis: Methods and Applications. *Camb. Camb. Univ. Press* (1994).

104. Vragović, I., E. Louis, & A. Díaz-Guilera. Efficiency of informational transfer in regular and complex networks. *Phys Rev E* (2005).

105. Csardi, G. & T. Nepusz. The igraph software package for complex network research. *Int. J. Complex Syst.* (2006).

106. Bonferroni, C. E. Teoria statistica delle classi e calcolo delle probabilità, Pubblicazioni del R Istituto Superiore di Scienze Economiche e Commerciali di Firenze 8, 3-62. **8**, 3–62 (1936).

107. Kleinberg, J. M. Authoritative sources in a hyperlinked environment. *J. ACM* **46**, 604–632 (1999).

108. Danecek, P. *et al.* The variant call format and VCFtools. *Bioinformatics* https://doi.org/10.1093/bioinformatics/btr330 (2011) doi:10.1093/bioinformatics/btr330.

109. Gompert, Z. & Buerkle, C. A. Bayesian estimation of genomic clines: BAYESIAN GENOMIC CLINES. *Mol. Ecol.* **20**, 2111–2127 (2011).

110. Benjamini, Y. & Hochberg, Y. Controlling the False Discovery Rate: A Practical and Powerful Approach to Multiple Testing. *J. R. Stat. Soc. Ser. B Stat. Methodol.* **57**, 289–300 (1995).

111. Chaudhry A. Mitochondria Analyzer [Software]. Available from: https://github.com/AhsenChaudhry/Mitochondria-Analyzer. (2019).

112. Rosseel Y. lavaan: An R package for structural equation modeling. *J. Stat. Softw.* **48**, 1–36 (2012).

Acknowledgments

Funding is provided by NIH R00 issued to DC and SUNY Research Foundation startup grant to SW.

Supplementary Materials

Table S1 Significant association between climate variables and OXPHOS gene expression.

	Effect Size	95% CI	*p_var*	R^2	*p_overall*
Prec_1970to2000	0.53	[0.32, 1.00]	10^{-6}	0.7239	10^{-8}
Prec_2024	0.56	[0.36, 1.00]	10^{-6}		
Species	0.20	[0.01, 1.00]	0.0266		
Temp_1970to2000	0.33	[0.12, 1.00]	0.0003	0.6228	10^{-5}
Temp_2024	0.35	[0.14, 1.00]	0.0002		
Species	0.39	[0.16, 1.00]	0.0003		
VP_1970to2000	0.70	[0.55, 1.00]	10^{-9}	0.7349	10^{-8}
VP_2024	0.26	[0.07, 1.00]	0.001674		
Species	0.06	[0.00, 1.00]	0.390305		

Table S2 Significant association between climate variables and ribosomal gene expression.

	Effect Size	95% CI	*p_var*	R^2	*p_overall*
Prec_1970to2000	0.40	[0.19, 1.00]	10^{-4}	0.5928	10^{-5}
Prec_2024	0.38	[0.17, 1.00]	10^{-4}		
Species	0.14	[0.00, 1.00]	0.07924		
Temp_1970to2000	0.14	[0.01, 1.00]	0.0267	0.4659	0.0003
Temp_2024	0.30	[0.10, 1.00]	0.0007		
Species	0.22	[0.03, 1.00]	0.0156		
VP_1970to2000	0.47	[0.26, 1.00]	10^{-5}	0.5448	10^{-4}
VP_2024	0.21	[0.04, 1.00]	0.0057		
Species	0.05	[0.00, 1.00]	0.4539		

Table S3 Significant association between climate variables and hemoglobin synthesis gene expression.

	Effect Size	95% CI	*p_var*	R2	*p_overall*
Prec_1970to2000	0.24	[0.06, 1.00]	0.0028	0.4997	10^{-3}
Prec_2024	0.36	[0.15, 1.00]	10^{-3}		
Species	0.10	[0.00, 1.00]	0.1693		
Temp_1970to2000	0.25	[0.06, 1.00]	0.0024	0.4432	10^{-3}
Temp_2024	0.17	[0.02, 1.00]	0.0124		
Species	0.20	[0.02, 1.00]	0.0236		
VP_1970to2000	0.50	[0.30, 1.00]	10^{-5}	0.5316	10^{-4}
VP_2024	0.10	[0.00, 1.00]	0.0621		
Species	0.01	[0.00, 1.00]	0.8459		

Table S4 The association between OXPHOS gene expression and glucose level in the blood cells.

Genes	Estimate	Standard Error	T value	*p* value	*p*_FDR
ATP5F1A	-0.0012	0.0117	-0.1017	0.9202	0.9641
ATP5MC3	0.0265	0.0603	0.4396	0.6661	0.9475
ATP5PB	0.0015	0.0061	0.2531	0.8034	0.9475
ATP6AP1	-0.0465	0.1782	-0.2609	0.7975	0.9475
ATP6V0C	-0.0073	0.0070	-1.0459	0.3112	0.9475
ATP6V0D1	0.0087	0.0195	0.4460	0.6616	0.9475
ATP6V0E2	-0.0029	0.0030	-0.9511	0.3557	0.9475
ATP6V1E1	0.0247	0.0101	2.4486	**0.0262**	0.5774
ATP6V1G3	0.0037	0.0044	0.8309	0.4183	0.9475
COX15	0.0484	0.0818	0.5915	0.5625	0.9475
COX5A	0.0123	0.0218	0.5654	0.5796	0.9475
COX5B	0.0023	0.0042	0.5595	0.5836	0.9475
COX6A1	0.0465	0.0522	0.8906	0.3864	0.9475
NDUFA10	0.0015	0.0083	0.1849	0.8556	0.9475
NDUFA8	-0.0038	0.0119	-0.3198	0.7533	0.9475
NDUFB10	0.0207	0.0191	1.0838	0.2945	0.9475
NDUFB3	0.0000	0.0058	0.0067	0.9948	0.9948
NDUFB8	-0.0017	0.0098	-0.1774	0.8614	0.9475
NDUFV2	-0.0095	0.0230	-0.4124	0.6855	0.9475
NDUFV3	0.0007	0.0030	0.2409	0.8127	0.9475
UQCRC1	0.0104	0.0064	1.6349	0.1216	0.9475
UQCRQ	-0.0313	0.0349	-0.8960	0.3835	0.9475

Table S5 The association between OXPHOS gene expression and triglyceride (TAG) level in the blood cells.

Genes	Estimate	Standard Error	T value	*p* value	*p*_FDR
ATP5F1A	0.1017	0.0296	3.4371	**0.0037**	**0.0403**
ATP5MC3	0.1327	0.2041	0.6500	0.5255	0.7756
ATP5PB	0.0391	0.0205	1.9060	0.0760	0.3344
ATP6AP1	0.2756	0.6135	0.4492	0.6597	0.8063
ATP6V0C	-0.0058	0.0254	-0.2303	0.8210	0.8900
ATP6V0D1	0.0391	0.0703	0.5565	0.5861	0.7756
ATP6V0E2	-0.0081	0.0105	-0.7754	0.4502	0.7756
ATP6V1E1	0.0255	0.0449	0.5680	0.5784	0.7756
ATP6V1G3	-0.0029	0.0152	-0.1930	0.8495	0.8900
COX15	0.1495	0.2785	0.5367	0.5993	0.7756
COX5A	0.2444	0.0466	5.2439	**$<10^{-4}$**	**0.0022**
COX5B	0.0140	0.0154	0.9042	0.3802	0.7756
COX6A1	0.4395	0.1542	2.8499	**0.0122**	0.0669
NDUFA10	0.0154	0.0286	0.5392	0.5977	0.7756
NDUFA8	0.0458	0.0395	1.1590	0.2646	0.6468
NDUFB10	0.2864	0.0936	3.0597	**0.0079**	0.0583
NDUFB3	0.0237	0.0276	0.8568	0.4050	0.7756
NDUFB8	0.0371	0.0319	1.1610	0.2638	0.6468
NDUFV2	-0.0219	0.0789	-0.2770	0.7856	0.8900
NDUFV3	-0.0156	0.0101	-1.5423	0.1438	0.4521
UQCRC1	0.0025	0.0235	0.1045	0.9182	0.9182
UQCRQ	0.1854	0.1115	1.6626	0.1172	0.4296

Table S6 The association between OXPHOS gene expression and ATP level in the blood cells.

Genes	Estimate	Standard Error	T value	*p* value	*p*_FDR
ATP5F1A	0.0000	0.0000	-0.5239	0.6061	0.8784
ATP5MC3	0.0000	0.0000	1.5039	0.1482	0.6901
ATP5PB	0.0000	0.0000	0.6346	0.5329	0.8784
ATP6AP1	0.0000	0.0000	0.2115	0.8346	0.9664
ATP6V0C	0.0000	0.0000	-1.9730	0.0625	0.6873
ATP6V0D1	0.0000	0.0000	0.7493	0.4624	0.8784
ATP6V0E2	0.0000	0.0000	-1.2674	0.2196	0.6901
ATP6V1E1	0.0000	0.0000	-0.0280	0.9780	0.9780
ATP6V1G3	0.0000	0.0000	0.0496	0.9610	0.9780
COX15	0.0000	0.0000	1.3353	0.1968	0.6901
COX5A	0.0000	0.0000	0.1510	0.8815	0.9696
COX5B	0.0000	0.0000	0.6527	0.5214	0.8784
COX6A1	0.0000	0.0000	0.7479	0.4632	0.8784
NDUFA10	0.0000	0.0000	0.5813	0.5676	0.8784
NDUFA8	0.0000	0.0000	0.9813	0.3382	0.8784
NDUFB10	0.0000	0.0000	-0.4765	0.6389	0.8784
NDUFB3	0.0000	0.0000	-1.2782	0.2158	0.6901
NDUFB8	0.0000	0.0000	-0.2325	0.8185	0.9664
NDUFV2	0.0000	0.0000	-2.5863	**0.0176**	0.3881
NDUFV3	0.0000	0.0000	-0.3979	0.6949	0.8993
UQCRC1	0.0000	0.0000	0.7432	0.4660	0.8784
UQCRQ	0.0000	0.0000	-1.4155	0.1723	0.6901

Table S7 The association between OXPHOS gene expression and NADPH/NADP$^+$ ratio in the blood cells.

Genes	Estimate	Standard Error	T value	*p* value	*p*_FDR
ATP5F1A	-0.0002	0.0001	-1.7790	0.0904	0.2487
ATP5MC3	-0.0004	0.0006	-0.5908	0.5613	0.7264
ATP5PB	-0.0002	0.0000	-4.1184	**0.0005**	**0.0059**
ATP6AP1	0.0003	0.0019	0.1484	0.8835	0.9150
ATP6V0C	0.0000	0.0001	-0.1081	0.9150	0.9150
ATP6V0D1	0.0004	0.0002	2.4411	**0.0241**	0.1163
ATP6V0E2	0.0000	0.0000	1.2898	0.2118	0.4215
ATP6V1E1	0.0000	0.0001	-0.2950	0.7710	0.8481
ATP6V1G3	0.0000	0.0000	0.3531	0.7277	0.8426
COX15	-0.0004	0.0009	-0.4699	0.6435	0.7866
COX5A	-0.0005	0.0002	-2.3349	**0.0301**	0.1163
COX5B	-0.0001	0.0000	-1.8960	0.0725	0.2279
COX6A1	-0.0012	0.0005	-2.3097	**0.0317**	0.1163
NDUFA10	-0.0001	0.0001	-0.7883	0.4398	0.6450
NDUFA8	-0.0001	0.0001	-0.9001	0.3788	0.6128
NDUFB10	-0.0007	0.0001	-5.1066	**0.0001**	**0.0012**
NDUFB3	-0.0001	0.0000	-2.3671	**0.0281**	0.1163
NDUFB8	-0.0001	0.0001	-0.8787	0.3900	0.6128
NDUFV2	-0.0002	0.0002	-1.2383	0.2299	0.4215
NDUFV3	0.0000	0.0000	1.3222	0.2010	0.4215
UQCRC1	0.0000	0.0001	0.5999	0.5553	0.7264
UQCRQ	-0.0004	0.0003	-1.2449	0.2276	0.4215